Proceedings of the 13th Annual Technical Conference on Composite Materials
September 21-23, 1998 Baltimore, Maryland

DEBONDING IN COMPOSITE SKIN/STRINGER CONFIGURATIONS UNDER MULTI-AXIAL LOADING

Michael K. Cvitkovich*, Ronald Krueger*, T. Kevin O'Brien**, and Pierre J. Minguet***
* National Research Council Research Associate
**U.S. Army Research Laboratory, Vehicle Technology Center
NASA Langley Research Center
Hampton, VA 23681
*** The Boeing Company
Philadelphia, PA 19142

ABSTRACT

The objective of this work was to investigate the damage mechanisms in composite bonded skin/stringer constructions under uniaxial and biaxial (in-plane/out-of-plane) loading conditions as typically experienced by aircraft crown fuselage panels. The specimens for all tests were identical and consisted of a tapered composite flange, representing a stringer or frame, bonded onto a composite skin. Tests were performed under monotonic loading conditions in tension, three-point bending, and combined tension/bending to evaluate the debonding mechanisms between the skin and the bonded stringer. For combined tension/bending testing, a unique servohydraulic load frame was used that was capable of applying both loads simultaneously. Microscopic investigations of the specimen edges were used to document the damage occurrence and to identify typical damage patterns. The observations showed that, for all three load cases, failure initiated in the flange near the flange tip causing the flange to almost fully debond from the skin.

A two-dimensional plain-strain finite element model was developed to analyze the different test cases using a geometrically nonlinear solution. For all three loading conditions, principal stresses exceeded the transverse strength of the material in the flange area. Additionally, delaminations of various lengths were simulated in the locations where delaminations were experimentally observed. The analyses showed that unstable delamination propagation is likely to occur at the loads corresponding to matrix ply crack initiation for all three loadings.

INTRODUCTION

Carbon epoxy composite structures are widely used by today's aircraft manufacturers to reduce weight. Co-curing, co-bonding, and secondary bonding have become the most promising processes to replace traditional mechanical fastening methods. Composite materials have been

introduced fairly recently into primary structures of commercial airplanes. The failure processes in composites are not as well understood as in metals. As of today, the majority of previous investigations related to failure of secondary bonded structures focused on uniaxial loading conditions only [1-4]. These loading conditions may be appropriate for a variety of applications, but in many cases composite structures may be loaded in more than one direction during in-flight service. The failure mechanisms under multi-axial loading may be complex in that they do not represent a simple combination of the various load components but involve interaction between the loads.

The first objective of this paper was to investigate the damage mechanisms in composite bonded skin/stringer structures under monotonic tension, three-point bending, and combined tension/bending loading conditions. For combined tension/bending testing, a unique servohydraulic load frame was used that was capable of applying axial tension and transverse bending loads simultaneously [5, 6]. Microscopic investigations of the specimen edges were performed to document the damage occurrence and to identify typical damage patterns.

The second objective was to develop an analytical methodology to accurately predict the experimentally observed damage occurrence. All three load cases were analyzed using a detailed two-dimensional plain-strain finite element model. Both linear and geometrically nonlinear simulations were performed. A stress analysis was used to predict the location and orientation of the first transverse crack based on the stress distribution in the flange tip area. A fracture mechanics approach was utilized to determine when a delamination will grow from this transverse crack. Mode I and mode II strain energy release rate contributions, G_I, and G_{II}, were calculated for all load cases using the virtual crack closure technique [7, 8] and compared to existing mixed-mode fracture toughness data.

EXPERIMENTAL INVESTIGATION

MATERIALS AND SPECIMEN PREPARATION

The specimens tested in this investigation consisted of a tapered flange, representing a composite stringer or frame, bonded onto a composite skin as shown in Figure 1. All specimens were machined from the same panels and were similar to the specimens used in the previous

monotonic and fatigue tests reported in references 2 through 4. Both the skin and the flange laminates had a multidirectional lay-up. The skin lay-up consisting of 14 plies was $[0/45/90/45/45/-45/0]_s$ and the flange lay-up consisting of 10 plies was $[45/90/-45/0/90]_s$.

Both skin and flange were made from IM6/3501-6 graphite/epoxy prepreg tape with a nominal ply thickness of 0.188 mm. First, the flange and skin laminates were cured separately. The flange parts were then cut into 50.0 mm long strips and machined with a 27° taper along the edges. Subsequently, the flange was adhesively bonded to the skin using a 177 °C cure film adhesive from American Cyanamid (CYTEC 1515). A grade-5 film was used to yield a nominally 0.127-mm thick bondline. However, because some of the adhesive flowed outwards during cure, the actual bondline thickness was 0. 102 mm. A diamond saw was used to cut the panels into 25.4-mm wide by 203.2-mm long specimens (the specimen length is the only difference to specimens used in previous studies [2-4] which were 127.0 mm long). Each specimen was then equipped with two strain gages, one located in the center of the flange and the

other located on the skin as close to the flange tip as possible. Ply properties and adhesive material properties are summarized in Table I. Specimen dimensions and strain gage positions are shown in Figure 1.

EXPERIMENTAL PROCEDURE

A total of five tension tests was performed in a servohydraulic load frame in displacement control. The actuator speed was controlled at 0.4 mm/min. The specimens were mounted in hydraulic grips to give a gage length of 127.0 mm as shown in Figure 2. An extensometer with a 25.4 mm gage length was mounted on the backside of the specimen and centered on the flange tip as displayed in Figure 2. The tests were terminated when the flange debonded from the skin.

A photograph of the three-point bending test fixture is shown in Figure 3. The configuration used was similar to the one used in previous studies [1, 3]. The bottom support had a 127.0 mm span. Mid-span deflections were recorded using a spring loaded direct current displacement transducer (DCDT) contacting the center of the flange as shown in Figure 3. Five specimens were tested in a servohydraulic load frame at a monotonic rate of 1.52 mm/min in accordance with previous four-point bending tests [2, 3]. The tests were stopped after the flange had debonded from the skin.

Tests under monotonic biaxial loading conditions were performed in a combined axial tension and bending (ATB) servohydraulic load frame shown in Figure 4. In this ATB load frame designed at the NASA Langley Research Center, the axial load cell is incorporated in the top grip that rotates with the upper specimen part (see close-up in Figure 5) [5, 6]. The specimens were mounted into the machine with great care placed on correct alignment of the specimen and the top grip/load cell set-up. The specimens were initially preloaded in load control to an axial tension load of 17.8 kN. While maintaining this preload, a transverse bending load was then applied in displacement control until flange debonding occurred. Maximum specimen deflections at the top grip contact point were recorded using a spring loaded linear variable differential transformer (LVDT).

The first specimen was tested with a gage length of 127.0 mm, and the four remaining specimens were tested with a gage length of 101.6 mm. The first specimen was equipped with eight strain gages, four on the skin and four on the flange. The transverse load was applied at a constant rate of 1.52 mm/min (in accordance with three- and previous four-point bending tests). As the stroke was increased, the specimen broke near the lower grip without flange debonding. As a result, the gage length was reduced to 101.6 mm which increased the bending moment at the lower flange tip so that flange debonding occurred before skin failure. The remaining specimens were equipped with two strain gages as described earlier. The transverse displacement rate was tripled to 4.57 mm/min to reduce testing time caused by the large specimen deflections necessary for damage initiation.

TEST RESULTS

In Figures 6 to 11, typical results of each test are shown as plots of load versus displacement and strain versus load. The strain-load curves are shown for flange strain and skin strain, respectively. The loads, flange and skin strains are reported in Tables II and III (tension

and three-point bending tests) for the point of possible damage initiation as well as for the maximum sustained load. In Table IV (ATB tests), the results are presented for the maximum sustained load only since no possible damage initiation prior to failure was observed in these tests.

For tension specimens, the load-displacement curves were nearly linear over a wide range as shown in Figure 6. Possible damage initiation was assumed when a small initial load drop was observed prior to flange debonding. At this point, a crack in one flange tip or even a small delamination along one flange corner was observed. In one specimen, no initial load drop or visible damage could be detected. In general, the initial load drop occurred above 90% of the maximum sustained load. Figure 7 shows the nonlinear strain-load response until flange debonding. In all specimens, a load drop was also accompanied by a decrease in strain.

Typical plots for the three-point bending tests are shown in Figures 8 and 9. The load versus mid-span deflection curves of all three-point bending specimens showed nonlinear behavior at higher loads indicating possible damage initiation sometimes accompanied by a minor load drop (see Figure 8). However, no visible cracks or delaminations could be observed prior to ultimate flange failure. In all specimens, the nonlinearity or initial load drop was again detected above 90% of the maximum sustained load. Both skin and flange strains showed linear behavior before flange debonding (see Figure 9). No initial drops in load or strain were observed.

In contrast to tension and three-point bending tests, the transverse load versus transverse displacement curves obtained from the ATB tests showed no indication of damage formation until just prior to skin failure for all specimens. Flange debonding could not be identified from these plots. A typical example is shown in Figure 10. Figure 11 shows a characteristic strain versus transverse load response. While Figure 11 shows linear behavior, the strain curves in some specimens deviated slightly from linearity prior to flange debonding. Flange debonding as detected during the experiments always occurred at maximum flange strain and was sometimes accompanied by a drop in skin strain.

MICROSCOPIC INVESTIGATION

After completion of all tests, photographs of the polished specimen edges were taken under a light microscope to document the occurrence of matrix cracks and delaminations. Damage was documented based on location at each of the four flange corners identified in Figure 12. Typical damage patterns observed from specimens are shown in Figure 13. These drawings are based on the micrographs taken after the tests. Figure 14 presents two such photomicrographs for a three-point bending specimen. All tests yielded similar damage patterns. In general, failure in tension and three-point bending specimens occurred on one side of the flange only, with no clear preference for either side (side 1 = corners 1 and 2; side 2 = corners 3 and 4). Due to the asymmetric nature of the ATB test, failure in ATB specimens occurred on the flange side with the higher bending moment only, i.e., the side closer to the lower grip.

At corners 1 and 4, a delamination running in the 90°/45° flange ply interface (delamination A) initiated from a matrix crack in the 90° flange ply as shown in Figure 13(a). At longer delamination lengths, new matrix cracks formed and branched into both the lower 45° as well as the upper 90° flange ply. However, no branching into the bondline was observed.

At corners 2 and 3, a split (delamination B 1) formed within the top 0° skin ply as depicted in Figure 13(b). It initiated at the flange tip from a matrix crack starting in the 90° flange ply that subsequently ran through the lower 45° flange ply and the bondline into the skin. In some cases, a second delamination (delamination B2) was observed below the first in the top 0°/45° skin ply interface. Both delaminations were present over a long distance until delamination B1 stopped and delamination B2 continued.

ANALYTICAL INVESTIGATION

FINITE ELEMENT ANALYSIS

The finite element (FE) method was used to analyze the test specimens for each loading case. The goal of this investigation was to study damage initiation using a stress analysis and the potential for delamination propagation using a fracture mechanics approach. FE models for an undamaged and two damaged specimens were developed and loads and boundary conditions were applied to simulate the three load cases. The two-dimensional cross section of the specimens was modeled using eight-noded quadrilateral plane strain elements using second order shape functions and reduced integration scheme. The models are shown in Figures 15 and 16. For the tension and three-point bending load cases, the ABAQUS geometric nonlinear analysis procedure was used. For both these loading cases, the results of the linear analyses were compared to those of nonlinear analyses. For the ATB test, only a nonlinear solution allowed the axial load to rotate with the specimen as it deformed under the transverse load and to account for the membrane stiffening effect caused by the axial load.

For the model of the undamaged specimen, a refined mesh was used in the critical area of the 90' flange ply where cracking was observed in the experiments. An outline and two detailed views of the mesh are shown in Figure 15. Outside the mesh refinement area, all plies were modeled with one element through the ply thickness. In the refined region, two elements were used per ply thickness with the exception of the first three individual flange plies above the bondline and the skin ply below the bondline which were modeled with four elements. Three elements through the thickness were used for the adhesive film. The model consisted of 6492 elements and 19975 nodes and had 39950 degrees of freedom.

Based upon the experimental observations shown in Figures 13 and 14, a “damaged” model was also developed that included discrete matrix cracks and delaminations. The mesh described for the undamaged specimen was also used for this model, with the exception of the critical area around the flange tip where delaminations were modeled as shown in Figure 16 (a) for corners 1 and 4 and Figure 16 (b) for corners 2 and 3. The initial matrix crack was modeled perpendicular to the flange taper. Each damage pattern was modeled on one flange side only. At the opposite taper, the mesh used in the model of the undamaged specimen was employed. This procedure was used to simulate the occurrence of damage onset only. It is inherent to a two dimensional plane strain FE model that the geometry, boundary conditions and other properties are constant through the entire width. This may not always capture the true nature of the problem. As shown in Figures 13 and 14, the delamination pattern changed from corner 3 to corner 4 from a delamination running in the 90°/45° interface to a delamination propagating between the

adhesive film and the top 0° ply of the skin. This three dimensional effect can not be accounted for in the current model.

The schematics of the specimen, boundary conditions, and loadings applied in the simulations are shown in Figure 17 for the tension and three point bending cases and in Figure 18 for the combined tension and bending case. For the tension and bending case, the mean loads reported for the point of possible damage initiation in Tables II and III were applied. At this point, possible damage initiation in the form of matrix cracks is likely to occur. For the simulation of the combined tension and bending loads in the ATB test, the top grip, the load cell, and the load pin were also modeled using three-noded quadratic beam elements as shown in Figure 18. A rectangular beam cross section was selected to model the square cross section of the top grip and load pin and a circular beam cross section was used for the model of the cylindrical load cell. The beams were connected to the two-dimensional plane strain model of the specimen using multi-point constraints to enforce appropriate translations and rotations as shown in Figure 18. To be consistent with the ATB tests, a constant axial load, P, was applied in a first load step while transverse loads remained zero. In a second load step, the axial load was kept constant while the load orientation rotated with the specimen as it deformed under the transverse load. In the FE simulation this transverse load was applied as a prescribed displacement which corresponded to the mean of the maximum transverse stroke (31 mm) reported in Table IV. The properties used to simulate the behavior of the graphite/epoxy material and the adhesive are given in Table I. For the beam model of the steel parts (top grip, load cell, and load pin), a Young's Modulus of 210 GPa and a Poisson's Ratio of 0.3 were used as material input data.

The Virtual Crack Closure Technique (VCCT) described in references 7 and 8 was used to calculate strain energy release rates for the delaminations. The mode I and mode II components of the strain energy release rate, G_I, and G_{II}, were calculated using the forces at the delamination tip, X_i' and Y_i' and the relative displacements behind the delamination tip, u_i' and v_i', as shown in Figure 19. Both forces and displacements were transformed into a local coordinate system (x', y'), that defined the normal and tangential coordinate directions at the deformed delamination tip. The total strain energy release rate, G_T was obtained by summing the individual mode components as $G_T = G_I + G_{II}$. The mode III component is zero for the plane strain case. These calculations were performed in a separate post processing step using nodal displacements and nodal forces at the local elements in the vicinity of the delamination front. The data required to perform the VCCT were accessed from the ABAQUS result file.

ANALYSIS RESULTS

Global Response

The load-displacement and the load-strain behavior computed for all three load cases were compared to the corresponding experimental results. This global response was used to examine whether the FE model, the boundary conditions, the loadings and the material properties used in the model were accurate. Note that the experimental data only represent one typical specimen, thus not accounting for any experimental scatter. Displacements were calculated at the locations where they were taken in the experiments. Strains were computed at a single location corresponding to the center of the strain gage. A schematic of the deformed geometries, the

boundary conditions, and the loadings applied in the simulations are shown in Figure 20 for all three load cases.

In the schematic of the deformed FE tension model in Figure 20(a), the elongation of the specimen caused by the applied tensile load is shown along with the bending effect caused by the load eccentricity. The load versus displacement plot in Figure 21 shows that the linear and nonlinear FE simulations are in good agreement. Moreover, there is little difference between the analyses and the experiments, thus confirming that the entire model was appropriate. In Figure 22, a comparison of experimentally measured strains and computed results is shown. The strain-load responses for the skin are again in good agreement between the experiments and both analyses. On the other hand, the linear analysis is not capable of calculating flange strains accurately. Hence, a geometrically nonlinear FE analysis is necessary to account for the local nonlinear behavior caused by the load eccentricity in the flange region.

In the three-point bending test, the vertical displacement at the flange tip (Figure 3) was of the order of the skin thickness for the load level investigated. Hence, a geometrically nonlinear FE solution procedure may also be needed in this case. Both linear and nonlinear analyses were performed and computed displacements and strains were compared. The load-displacement plot in Figure 23 and the strain-load plot in Figure 24 show that both simulations and the experiments are within 10% of each other. Consequently, a linear analysis is sufficient for the load level investigated, i.e., the mean load found experimentally for possible damage initiation. Higher load levels, however, might require a nonlinear analysis.

Based upon the large displacements observed in the ATB, only the nonlinear FE solution procedure was chosen for this simulation. The load-displacement and strain-load plots in Figures 25 and 26 show that the nonlinear FE simulation and the experiments are again in reasonable agreement, i.e., within 20% of each other.

Local Response

The local response was studied in the critical area of the 90° flange ply where cracking was observed in the experiments. The goal of these FE analyses was to investigate damage initiation using a stress analysis and the potential for delamination propagation using a fracture mechanics approach.

The stress analysis was used to analyze the initial failure in the form of matrix cracks from which delaminations may start to grow. As shown in Figures 13 and 14, the first crack always occurred in the 90° flange ply closest to the skin. The previous investigations [3, 4] suggested that the maximum ply transverse tensile stress may cause this initial failure. Failure, therefore, may occur when the computed principal tensile stress in the ply 2-3 plane exceeds the transverse strength of this ply. In this model, the ply 2-3 plane for a 90° ply coincides with the global x-y plane of the model. Maximum principal stresses can therefore be taken straight from the finite element results. The vector plot in Figure 27 shows the trajectories of the maximum principle tensile stresses in the flange ply. At the -45°/90° and 90°/45° interface multiple vectors are displayed since the stresses were not averaged across boundaries for elements with different material properties. Comparing the trajectories in Figure 27 with the damage patterns shown in Figures 13 and 14 shows that the crack starts to grow perpendicular to the trajectory of the maximum principle stress. Computed maximum principal stresses in the elements with labeled

element numbers in the 90° ply in Figure 27 are presented in Table V and compared in Figure 28. For all three loading conditions, computed maximum principal tensile stresses have similar magnitudes. Towards the center of the ply, principal stresses exceeded the failure strength of 61.1 MPa (as found for a similar type of material (AS4/3501-6) in [10]) and hence ply cracks can develop. Consequently, the stress analysis based on the comparison of computed stresses with failure strengths appears to be an appropriate method to determine the location of the initial failure and the orientation of the resulting crack.

A fracture mechanics approach was used to investigate delamination growth once the initial crack had formed. The initial crack was modeled on one flange side perpendicular to the flange taper as suggested by the microscopic investigation and the stress analysis described in the previous paragraph. Recall that the models of the discrete cracks and delaminations are shown in Figure 16. During the analyses, the delaminations were extended by adding new nodes at the crack tip and in front of the crack tip. These nodes were then assigned to the elements on one side of the crack thus creating a row of disconnected elements which simulated the delamination. Strain energy release rates were computed for each tip location. The delamination lengths, a, are measured from the end of the initial matrix crack as shown in Figure 16. The results at corners 1 and 4 (delamination in the 90°/45° flange ply interface) are plotted in Figures 29 through 31 for all the three loading conditions. Initial mode I and mode II values of all three cases are similar. In Figures 29 through 31, G_{II}, for all load cases increases monotonically while G_I begins to level off. Plots of computed strain energy release rates with increasing delamination length for the simulated delamination propagation along the 0° skin ply/adhesive film interface are given in Figures 32 through 34. The computed values at delamination onset (a = 0.04 mm, i.e., delamination length equal to one element length as seen in Figure 16) are given in Table VII. Comparing all load cases, computed G_I results appear to have similar magnitudes. Mode II values, however, differ noticeably. As shown in Figures 32 through 34, at $a < 0.2$ mm the mode I contribution decreases with increasing delamination length. The mode II contribution and the total energy release rate, however, increase with increasing delamination length. At $a > 0.2$ mm, all three strain energy release rates level off. The results discussed above will be used in a mixed-mode failure investigation to determine whether delamination onset and unstable propagation are possible at the applied loads where damage was observed in the experiments.

MIXED-MODE FAILURE INVESTIGATION

Accurate mixed-mode failure criteria are necessary for the prediction of delamination growth. A bilinear mixed-mode failure criterion was suggested in reference 10 for AS4/3501-6, a material similar to IM6/3501-6. The mixed-mode failure response was presented by plotting the mode I component of the mixed-mode fracture toughness versus the respective mode II component. A different approach to present the data was suggested in reference 11 where mixed-mode fracture toughness values, G_c, were plotted versus the mixed mode ratio G_{II}/G_T (see Figure 35). When this ratio is zero, G_c is simply the mode I fracture toughness, G_{Ic}. Alternatively, G_c becomes the mode II fracture toughness, G_{IIc}, when the mixed-mode ratio equals unity. An equation resulting from a least square regression cubic curve fit to these data defines the mixed-mode delamination fracture criterion for each ratio as:

$$G_c = 75.3 + 214.7\left(\frac{G_{II}}{G_T}\right) - 70.5\left(\frac{G_{II}}{G_T}\right)^2 + 327.4\left(\frac{G_{II}}{G_T}\right)^3 \quad (1)$$

Hence, for a given mixed-mode ratio, growth is possible when the total mixed-mode energy release rate exceeds the critical value.

In the current study, computed total strain energy release rates, G_T, were compared to the critical value, G_c, for the appropriate mixed mode ratio (G_{II}/G_T) for each load case in order to determine the potential for delamination growth. Values calculated for delamination onset in the 90°/45° flange ply interface are below the fracture toughness data as shown in Table V and Figure 36. Consequently, onset is unlikely to occur at the load corresponding to possible damage initiation for all three tests. Propagation in the 0° skin ply/adhesive film interface, on the other hand, will occur in all three cases as the computed results are much higher than the reported fracture toughness values as shown in Table VI and Figure 37. Unstable propagation is likely since the calculated G_T-values increase and remain above the mixed-mode fracture toughnesses over the entire simulated length as shown in Figures 30 to 32. This assumption is confirmed by the experimental results of this study.

The above findings suggest that once a matrix crack has formed, a delamination (delamination B1 from Figure 14) will also form and grow in an unstable manner between the adhesive film and the top 0° skin ply. The second delamination found experimentally in the 90°/45° flange ply interface (delamination A from Figure 14) requires more energy to initiate than available at the load levels used in this FE analysis, i.e., the loads corresponding to possible matrix ply crack initiation. The energy for this second delamination may come from an increase in load or may be caused by an increase in G due to the presence of the delamination in the 0° skin ply/adhesive film interface.

CONCLUDING REMARKS

The damage mechanisms in composite bonded skin/stringer constructions under uniaxial and biaxial (in-plane/out-of-plane) loading conditions have been investigated using experimental and numerical approaches. Tests were performed under monotonic loading conditions in tension, three-point bending, and combined tension/bending to evaluate the debonding mechanisms between the skin and the bonded stringer or frame. Microscopic investigations of the specimen edges showed that all tests yielded similar damage patterns. For all three load cases, failure initiated in the flange, near the flange tip, causing part of the flange to fully debond from the skin.

Based upon the experimental findings, a two-dimensional nonlinear plain-strain finite element (FE) analysis was performed using the ABAQUS FE code. For tension and three-point bending tests, linear and geometrically nonlinear simulations were performed. Overall, both computed results were found to be in good agreement with the experimental data, thus confirming that the entire model was suitable. To account for the large displacements observed in the ATB tests, only the geometrically nonlinear analysis was performed. Again, the results were in good agreement with the experiments.

A stress analysis was used to investigate the onset of failure. This approach showed that the location and orientation of the initial transverse ply crack in the flange is dependent on the stress distribution in the critical area near the flange tip. For all three loading conditions, computed maximum principal tensile stresses were almost identical and exceeded the failure strength. A fracture mechanics approach was used to determine the potential for delamination growth from the initial transverse crack. In this approach, delaminations of various lengths originating from the transverse crack as observed in the experiments are simulated. Mode I and mode II strain energy release rate contributions were calculated for all load cases using the virtual crack closure technique. Computed total strain energy release rates were compared to critical values obtained from an existing mixed-mode failure criterion. The results suggest that once a matrix ply crack has initiated in the flange, a delamination will form and grow in an unstable manner between the adhesive film and the top 0° skin ply as observed in the micrographs. A second delamination found experimentally in the 90°/45° flange ply interface requires more energy to initiate than available at the load levels used in the FE analysis.

ACKNOWLEDGMENTS

This work was performed as part of a Cooperative Research and Development Agreement (CRDA) between the U.S. Army Research Laboratory, Vehicle Technology Center, and Boeing, Philadelphia.

REFERENCES

[1] Minguet, P.J., “Analysis of the Strength of the Interface between Frame and Skin in a Bonded Composite Fuselage Panel,” Proceedings of the 38th AIAA/ASME/ASCE/AHS/ASC SSDM Conference and Exhibit, Kissimmee, Florida, 1997, AIAA-97-1342, pp. 2783-2790.

[21 Minguet, P.J. and O’Brien, T.K., “Analysis of Composite Skin/Stringer Bond Failures Using a Strain Energy Release Rate Approach,” Proceedings of the Tenth International Conference on Composite Materials, Vol. 1, Woodhead Publishing Ltd., 1995, pp. 245-252.

[3] Minguet, P.J. and O’Brien, T.K., “Analysis of Test Methods for Characterizing Skin/Stringer Debonding Failures in Reinforced Composite Panels,” *Composite Materials: Testing and Design, Twelfth Volume,* ASTM STP 1274, August 1996, pp. 105-124.

[4] Cvitkovich, M.K., O’Brien, T.K., and Minguet, P.J., “Fatigue Debonding Characterization in Composite Skin/Stringer Configurations,” NASA TM 11033 1, April 1997.

[51 O'Brien, T.K., Murri, G.B., Hagemeier, R., and Rogers, C., "Combined Tension and Bending Testing of Tapered Composite Laminates," *Applied Composite Materials,* 1, 1995, pp. 401-413.

[6] Murri, G.B., O'Brien, T.K., and Rousseau, C.Q., "Fatigue Life Methodology for Tapered Composite Flexbeam Laminates," *Journal of the American Helicopter Society,* Vol. 43, (2), Apr 1998, pp. 146-155.

[7] Rybicki, E.F. and Kanninen, M.F., "A Finite Element Calculation of Stress Intensity Factors by a Modified Crack Closure Integral," *Eng. Fracture Mech.,* 9, 1977, pp. 931-938.

[81 Raju, I.S., "Calculation Of Strain-Energy Release Rates With Higher Order And Singular Finite Elements," *Eng. Fracture Mech.,* 28, 1987, pp. 251-274.

[91 O'Brien, T.K., Murri, G.B., and Salpekar, S.A., "Interlaminar Shear Fracture Toughness and Fatigue Thresholds for Composite Materials," *Composite Materials: Fatigue and Fracture, Second Volume,* ASTM STP 1012, 1989, pp. 222-250.

[10] Reeder, J.R., 'A Bilinear Failure Criterion for Mixed-Mode Delamination," *Composite Materials: Testing and Design, Eleventh Volume,* ASTM STP 1206, 1993, pp. 303-322.

[11] O'Brien, T.K., "Composite Interlaminar Shear Fracture Toughness, Glj,: Shear Measurement or Sheer Myth?," NASA TM 110280, February 1997.

TABLE I. MATERIAL PROPERTIES.

IM6/3501-6 Unidirectional Graphite/Epoxy Tape		
E_{11} = 144.7 GPa	E_{22} = 9.65 GPa	E_{33} = 9.65 GPa
ν_{12} = 0.30	ν_{13} = 0.30	ν_{23} = 0.45
G_{12} = 5.2 GPa	G_{13} = 5.2 GPa	G_{23} = 3.4 GPa

CYTEC 1515 Adhesive		
E = 1.72 GPa	ν = 0.30	(assumed isotropic)

TABLE II. RESULTS FOR TENSION TESTS.

Specimen	Damage initiation load kN	Damage initiation flange strain με	Damage initiation skin strain με	Max. load kN	Flange strain at max. load, με	Skin strain at max. load, με
2	20.5	5449	5619	22.8	1348	6084
4	21.8	1419	6312	23.6	1231	6685
6	19.9	1185	5834	23.1	1187	6599
8	20.9	1300	6051	23.0	1115	6463
10	21.1	1360	6092	21.1	1360	6092
Mean	20. 9	1298	5982	22.7	1248	6385
Std. Dev.	0.7	96	264	0.9	105	282
CoV, %	3.3	7.4	4.4	4.2	8.4	4.4

TABLE III. RESULTS FOR THREE-POINT BENDING TESTS.

Specimen	Damage initiation load kN	Damage initiation flange strain με	Damage initiation skin strain με	Max. load kN	Flange strain at max. load, με	Skin strain at max. load, με
11	404	3207	3811	440	3508	4160
13	433	3051	3691	484	3405	4110
15	445	3231	3659	468	3408	3868
17	425	3036	3657	434	3103	3701
19	431	3023	3481	488	3428	3945
Mean	428	3110	3660	463	3370	3957
Std. Dev.	14.9	101	118	24.4	155	186
CoV, %	3.5	3.2	3.2	5.3	4.6	4.7

TABLE IV. RESULTS FOR ATB TESTS.

Specimen	Max. transverse load, kN	Max. transverse stroke, mm	Flange strain at max. transverse load, με	Skin strain at max. transverse load, με
12	2.8	31.6	1318	7199
14	-	-	-	-
16	2.9	33.2	1232	7254
18	2.9	33.9	1276	7295
20	2.2	25.1	1278	7015
Mean	2.7	31.0	1276	7191
Std. Dev.	0.3	4.0	35	124
CoV, %	11.6	13.0	2.8	1.7

axial load = 17.8 kN

TABLE V. RESULTS FOR FINITE ELEMENT STRESS ANALYSIS.

Specimen	Element 1584 σ_{max}, MPa	Element 1604 σ_{max}, MPa	Element 1624 σ_{max}, MPa	Element 1644 σ_{max}, MPa
Tension	51.4	70.2	87.7	100.9
Bending	46.7	62.9	78.0	89.8
ATB	65.0	93.1	119.7	139.0

for comparison, transverse tensile strength: 61.1 MPa for AS4/3501-6 [10]

TABLE VI. RESULTS FOR DELAMINATION GROWTH IN 90°/45°INTERFACE.

Specimen	G_I, J/m^2	G_{II}, J/m^2	G_T, J/m^2	G_{II}/G_T	G_c, J/m^2
Tension	53.4	13.3	66.7	0.200	118
Bending	42.4	10.2	53.0	0.200	118
ATB	67.3	24.1	91.4	0.260	132

TABLE VII. RESULTS FOR DELAMINATION GROWTH IN FILM/0°INTERFACE.

Specimen	G_I, J/m^2	G_{II}, J/m^2	G_T, J/m^2	G_{II}/G_T	G_c, J/m^2
Tension	362	76.8	439	0.175	112
Bending	272	39.0	311	0.125	101
ATB	358	191	549	0.349	155

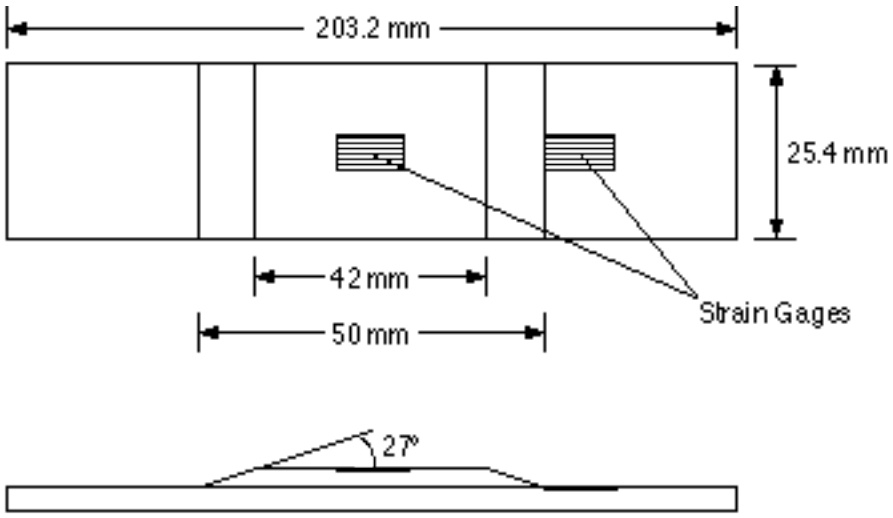

Figure 1. Specimen Configuration.

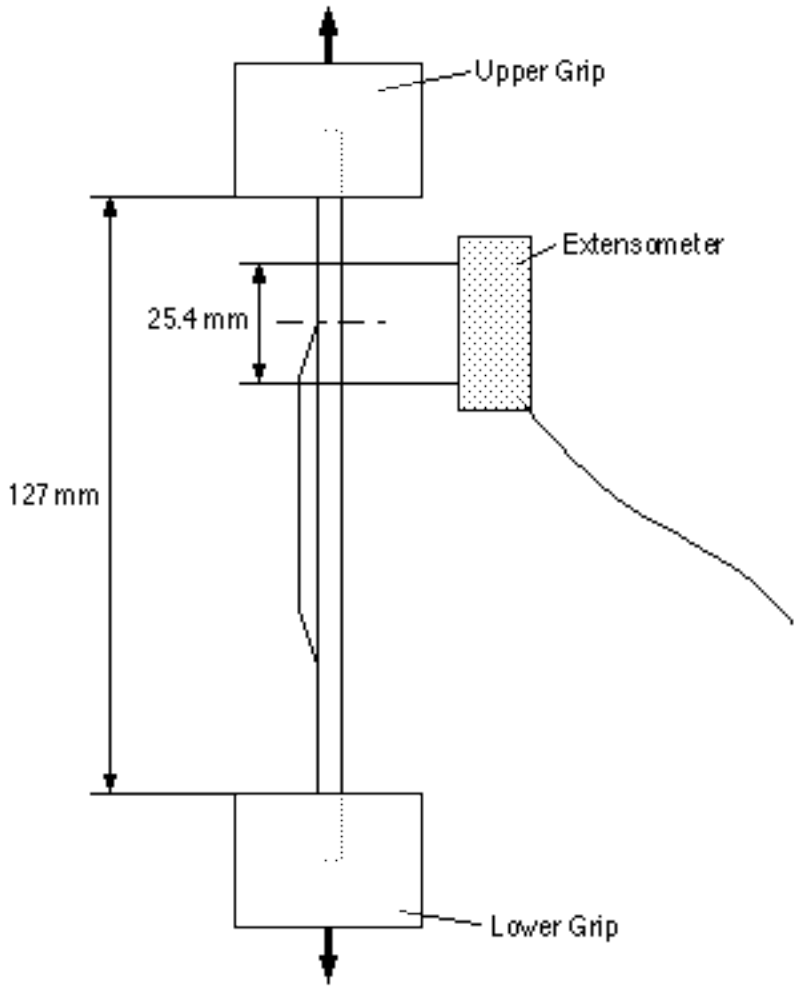

Figure 2. Tension Test Set-Up.

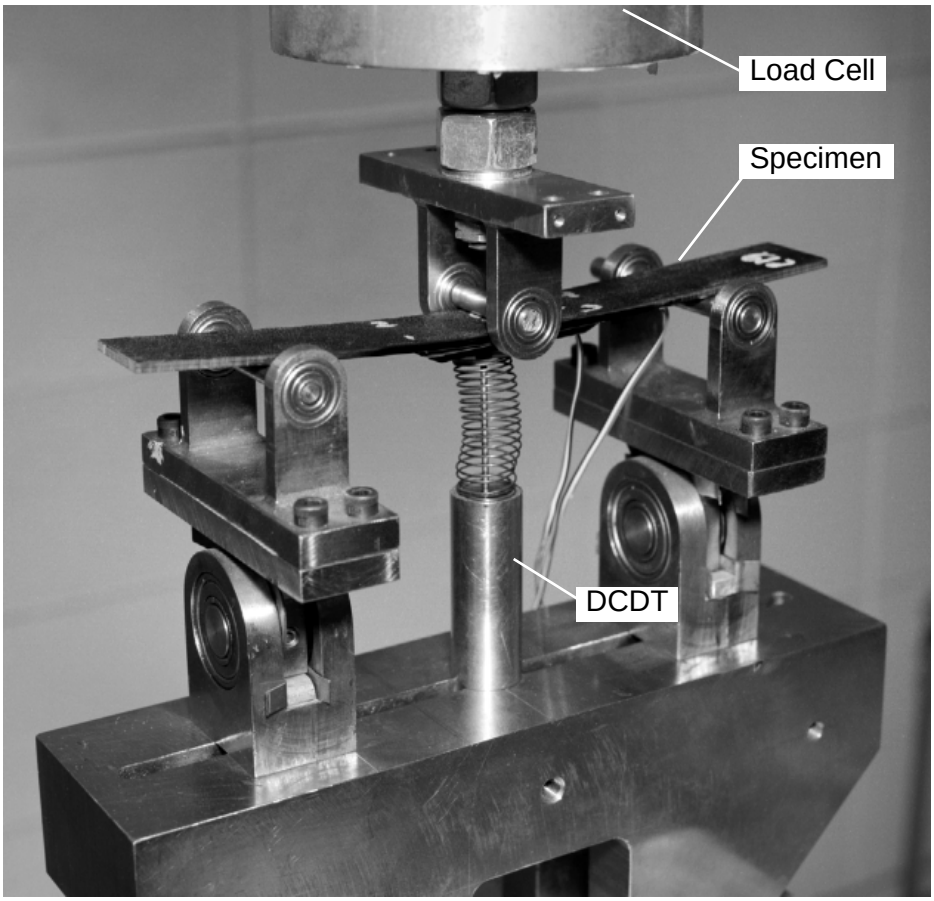

Figure 3. Three-Point Bending Test Set-Up.

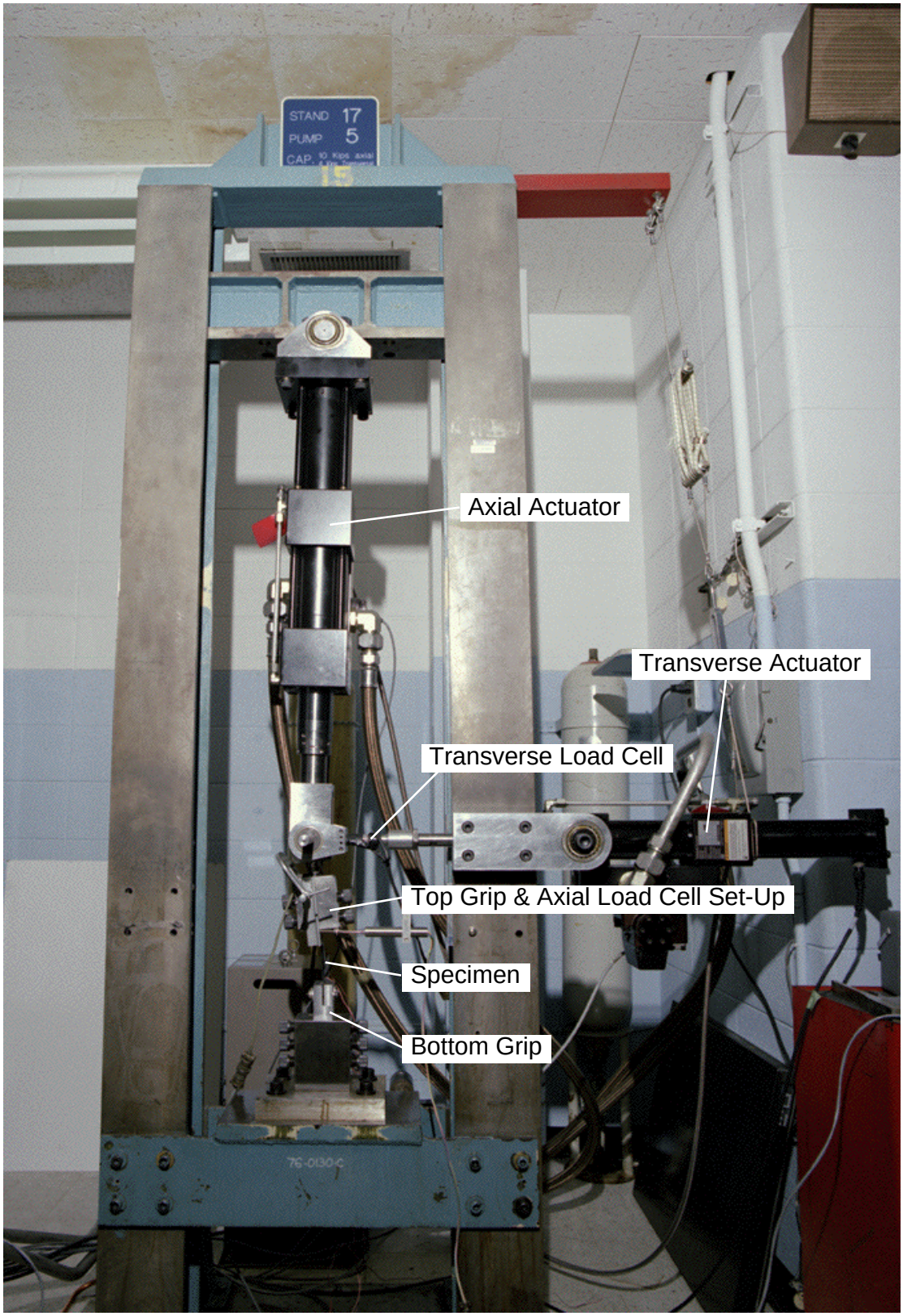

Figure 4. ATB Test Set-Up.

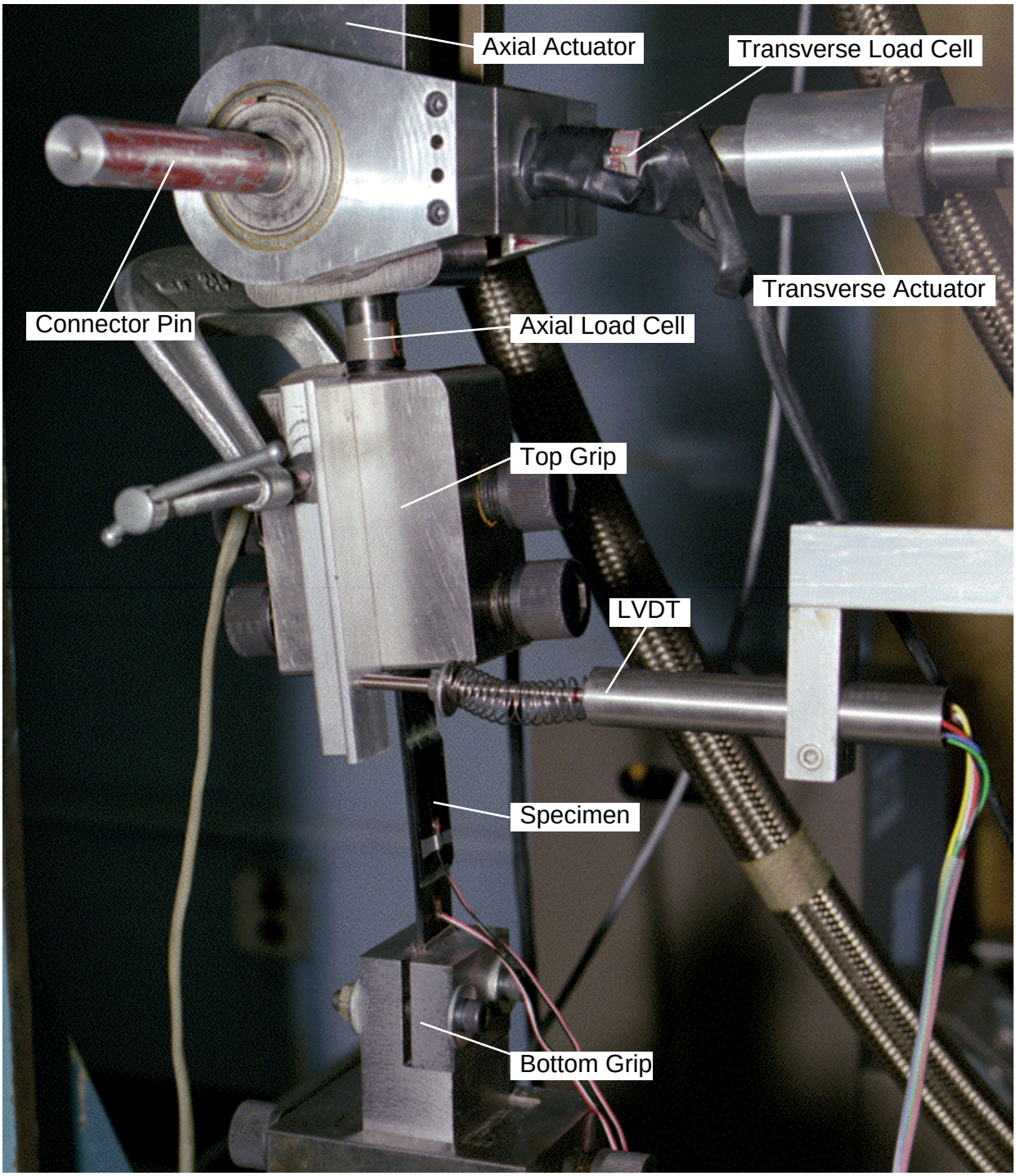

Figure 5. ATB Test Set-Up Close View.

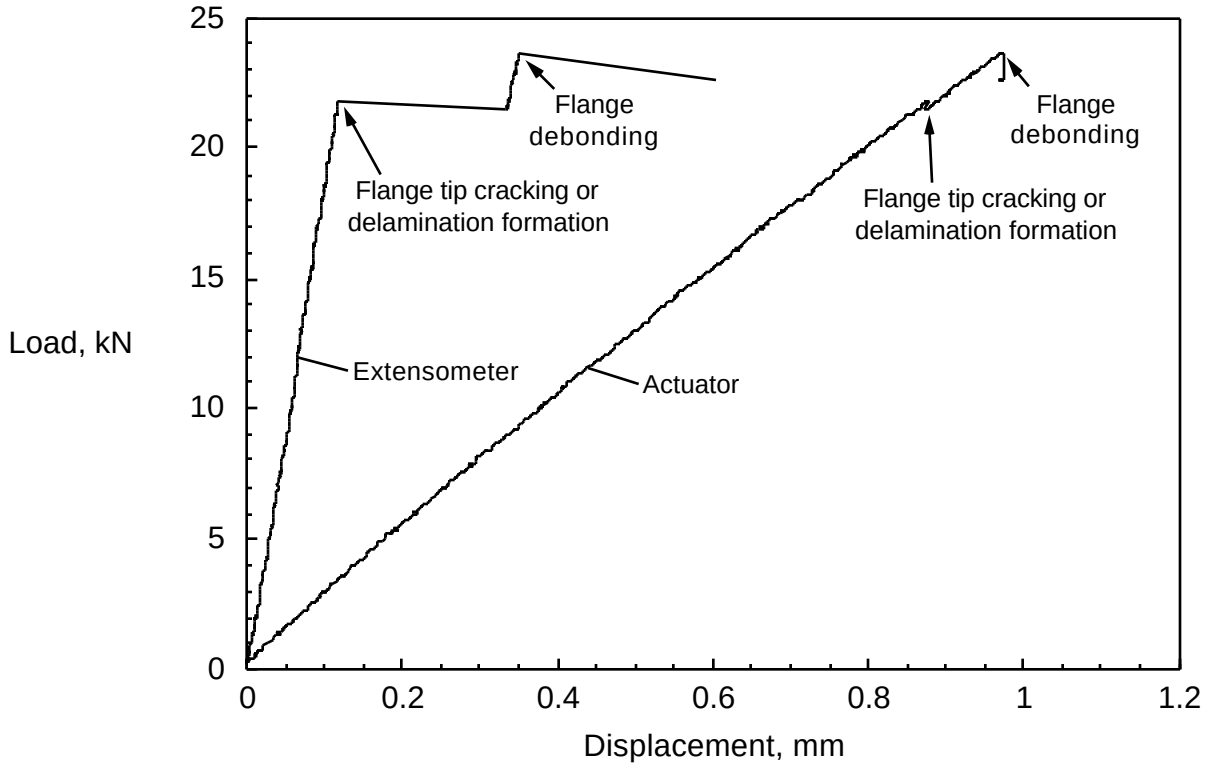

Figure 6. Typical Load-Displacement Plot for Tension Tests.

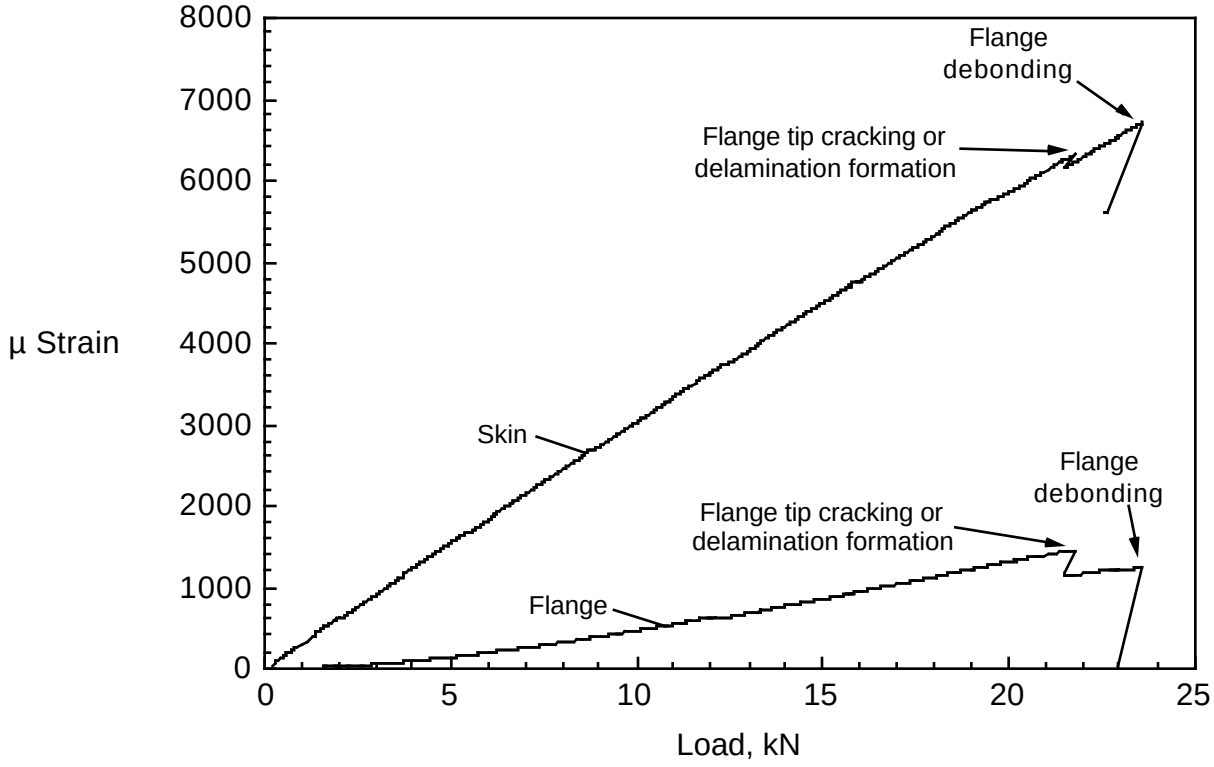

Figure 7. Typical Strain-Load Plot for Tension Tests.

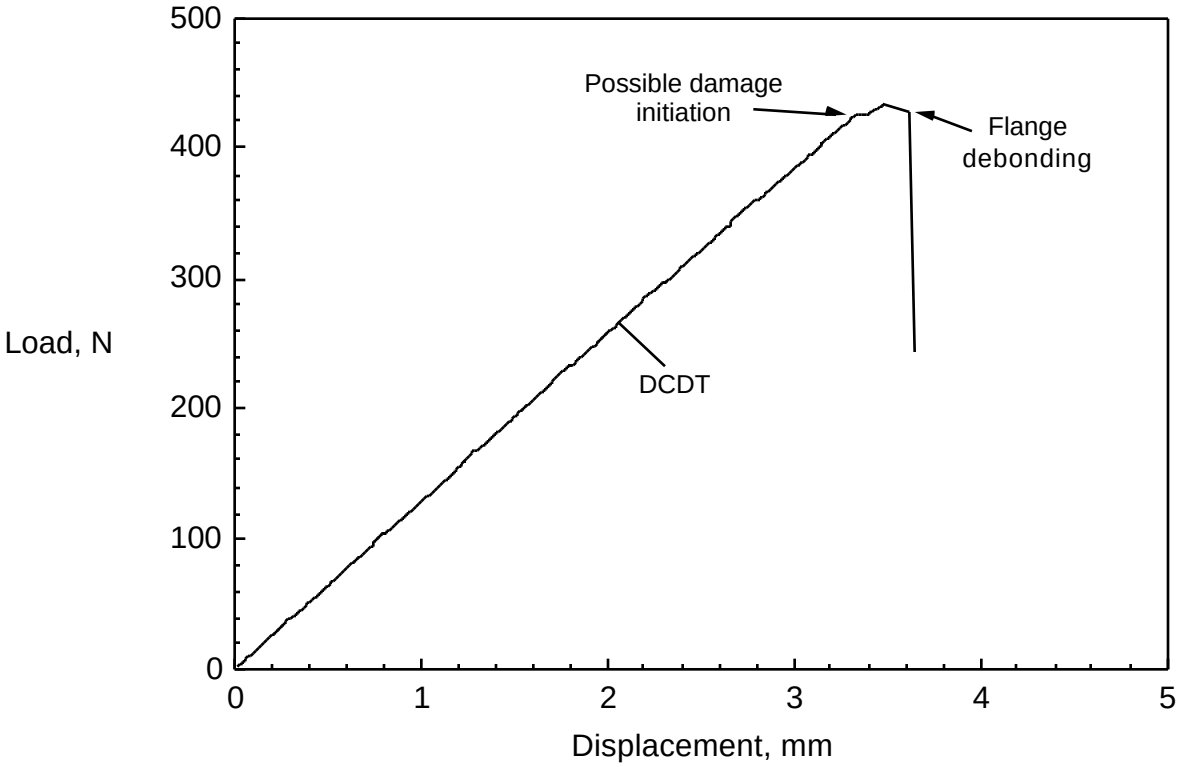

Figure 8. Typical Load-Displacement Plot for Three-Point Bending Tests.

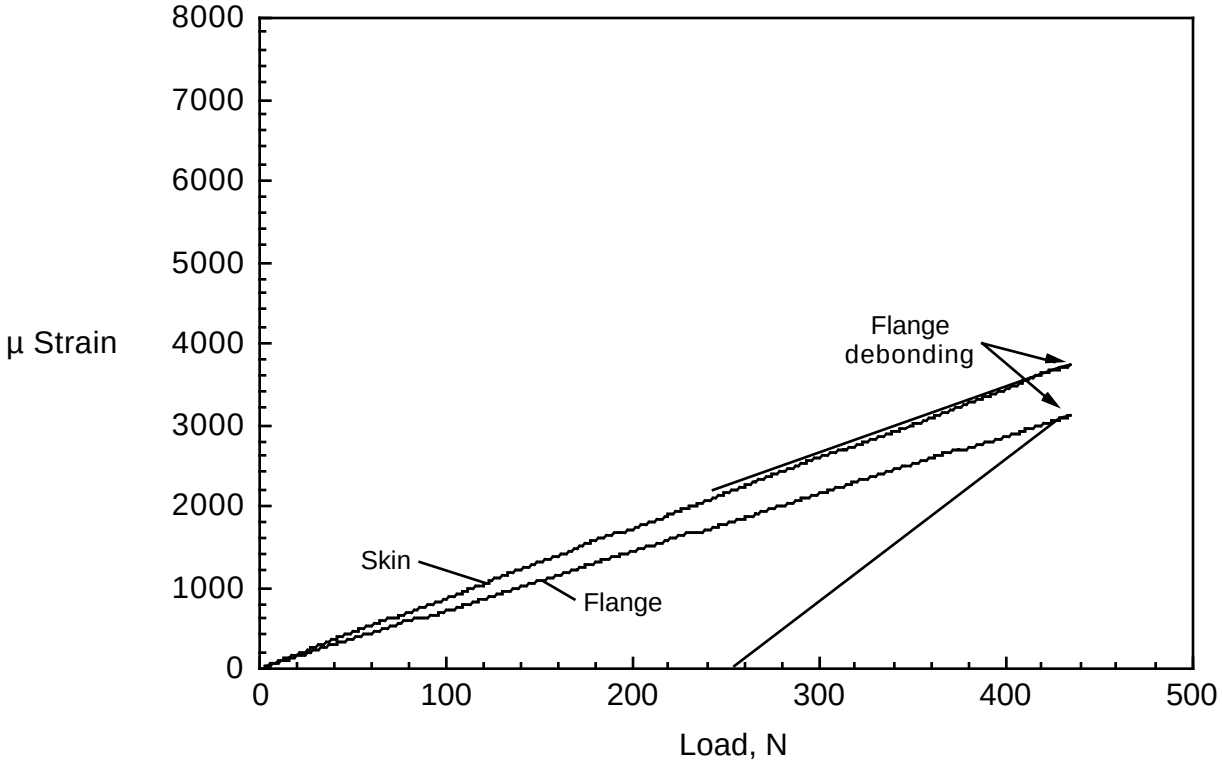

Figure 9. Typical Strain-Load Plot for Three-Point Bending Tests.

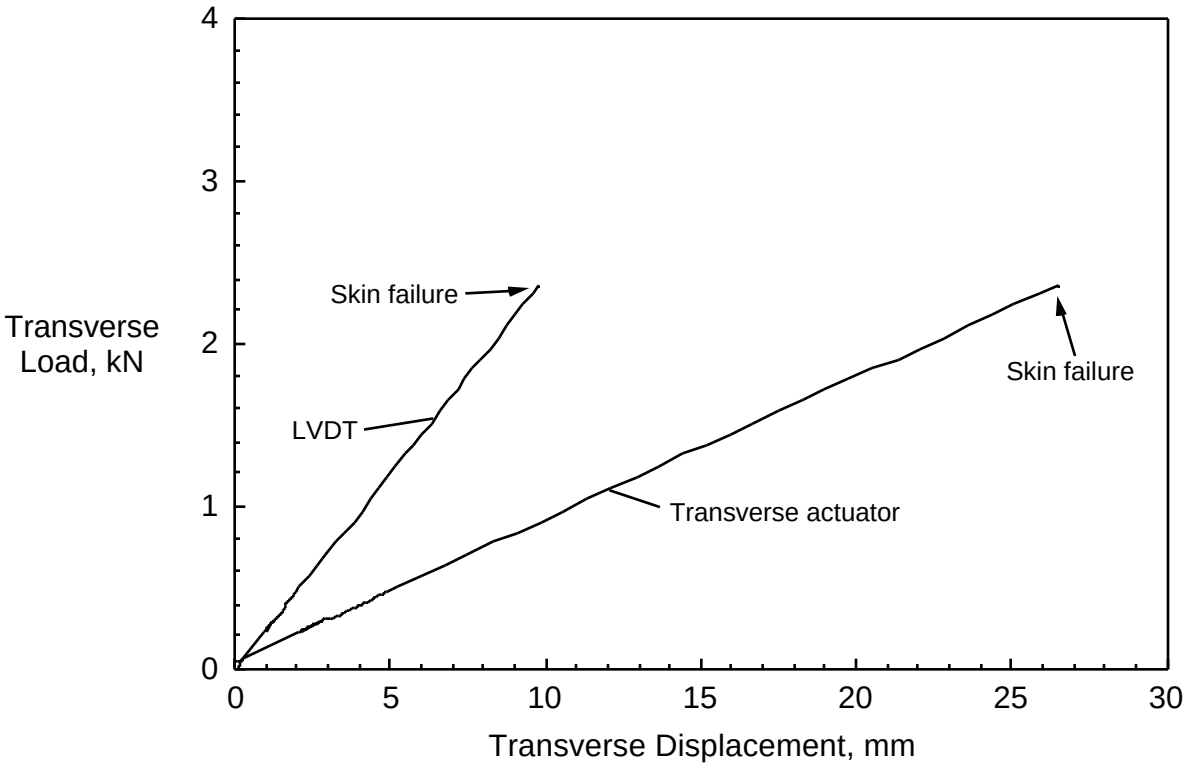

Figure 10. Typical Load-Displacement Plot for ATB Tests.

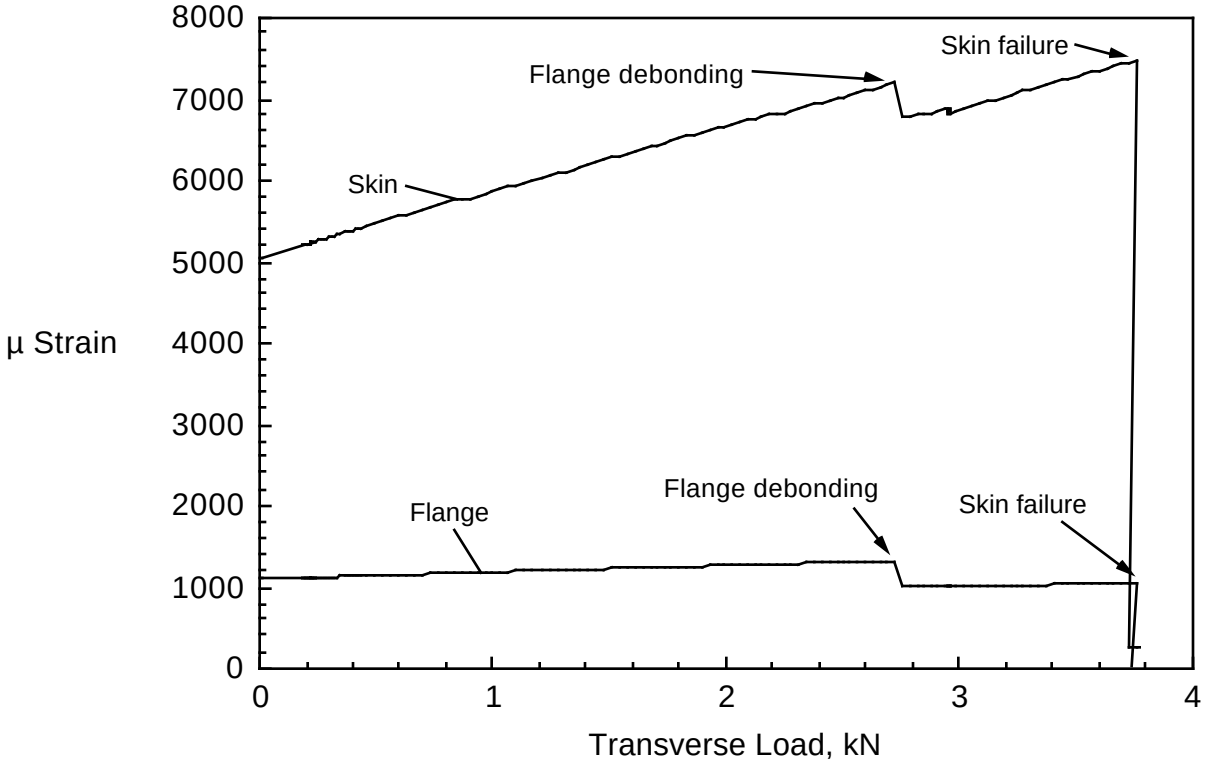

Figure 11. Typical Strain-Load Plot for ATB Tests.

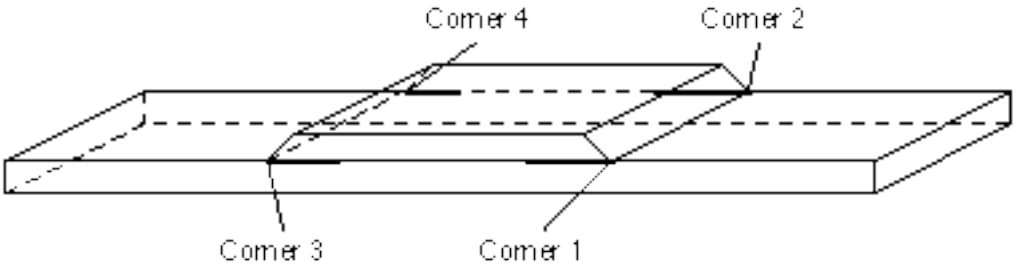

Figure 12. Specimen with Crack Locations.

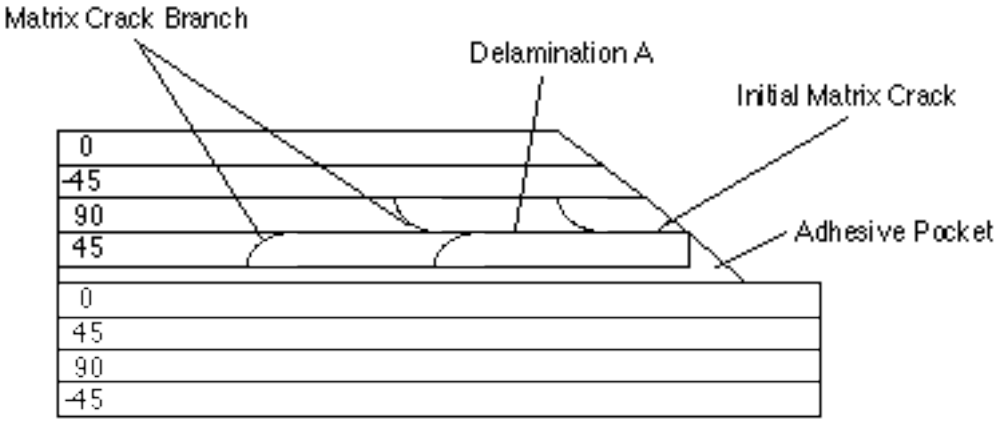

(a) Corners 1 and 4

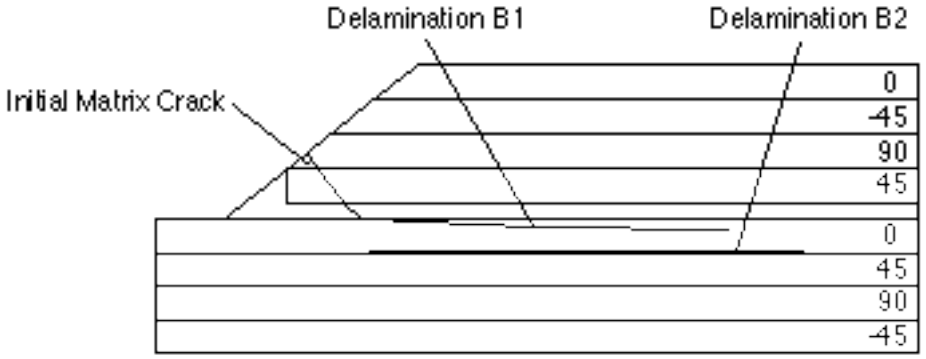

(b) Corners 2 and 3

Figure 13. Typical Damage Patterns.

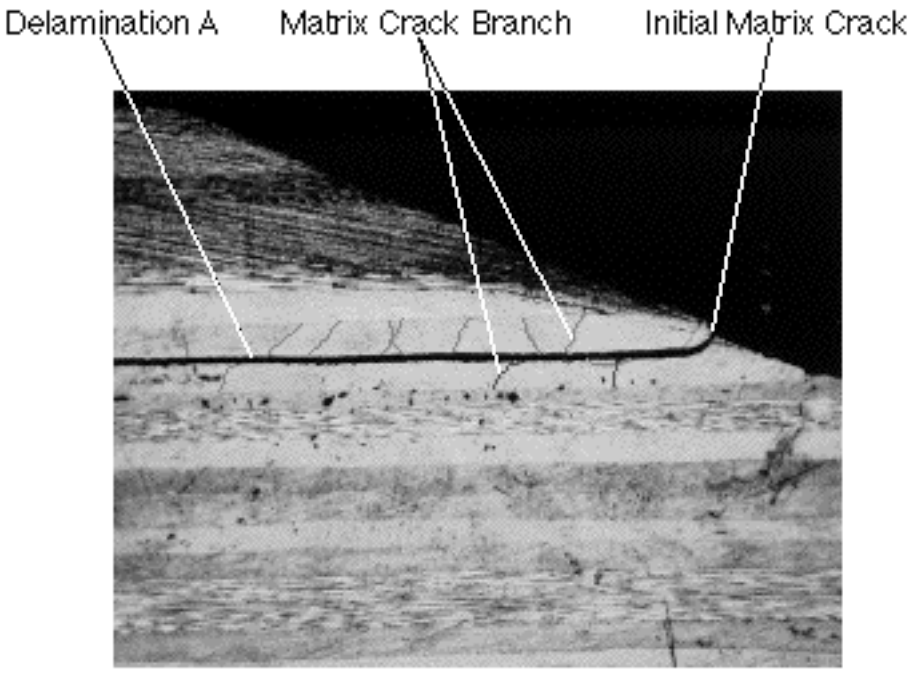

(a) Delamination A in the 90°/45° Flange Ply Interface at Corner 4

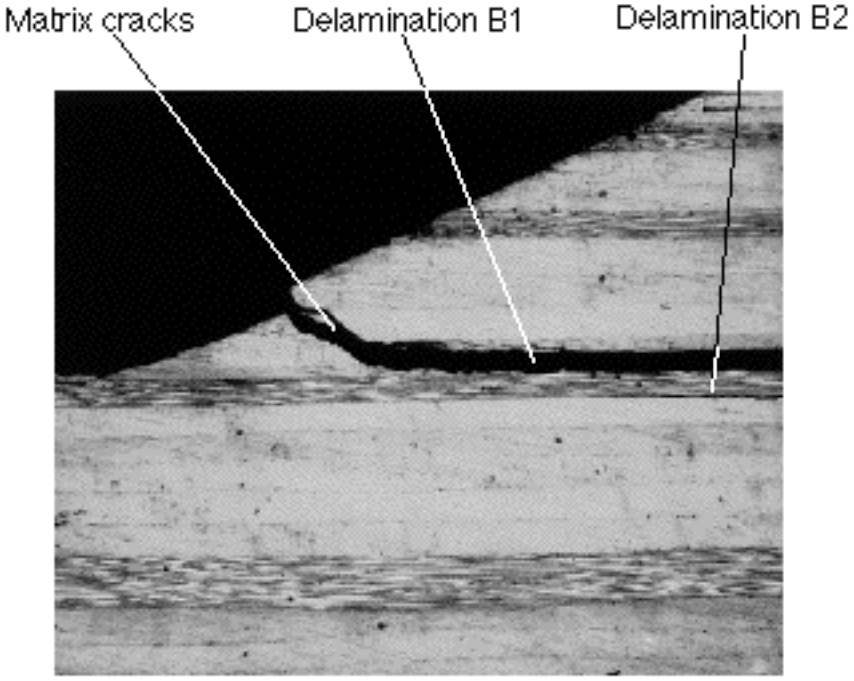

(b) Delamination B1 in the Top 0° Skin Ply and Beginning of Delamination B2
the top 0°/45° Skin Ply Interface at Corner 2

Figure 14. Micrograph showing the Side View of a Failed Three-Point Bending Specimen.

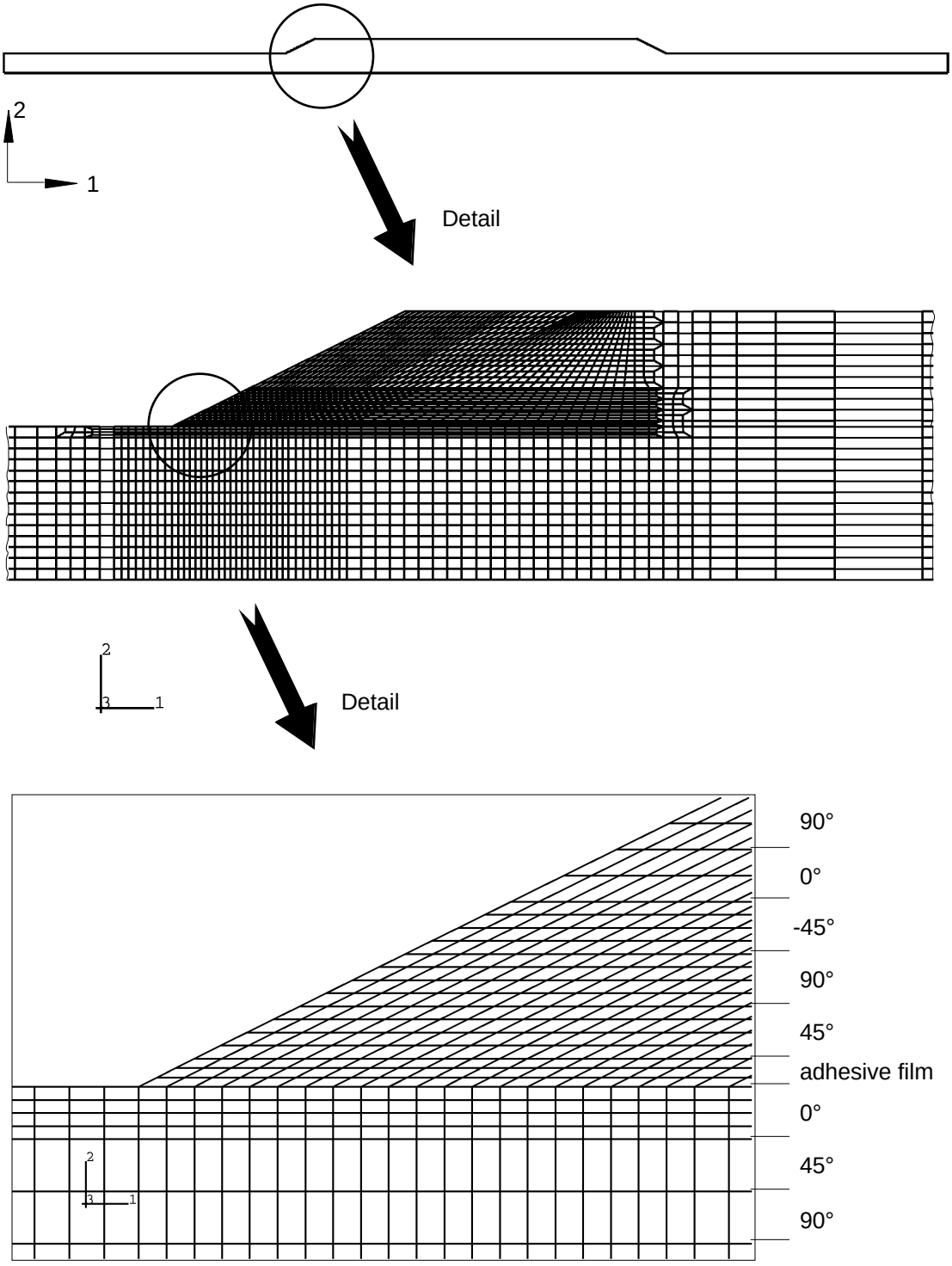

Figure 15. Finite Element Model of an Undamaged Specimen.

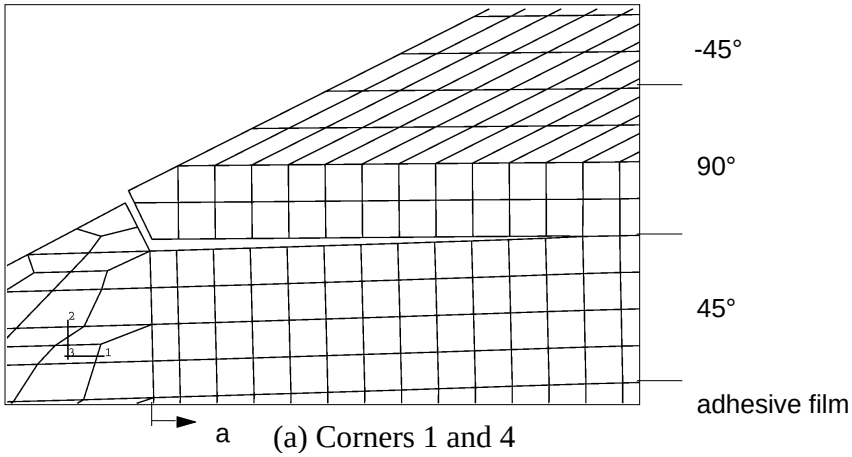

(a) Corners 1 and 4

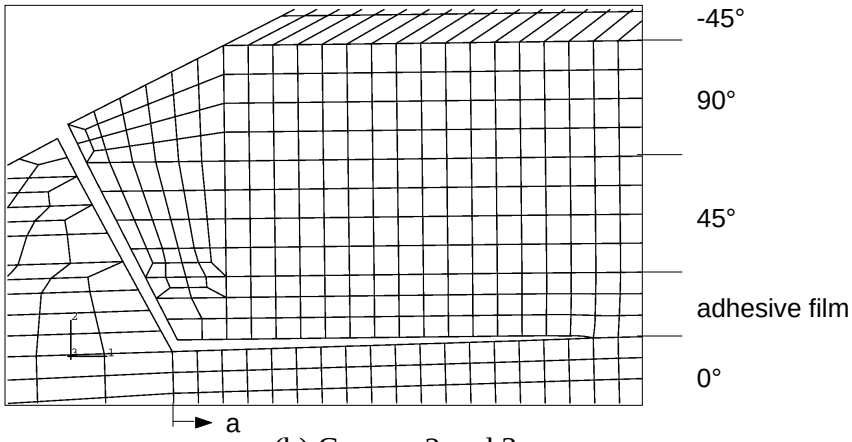

(b) Corners 2 and 3

Figure 16. Modeled Damage Patterns.

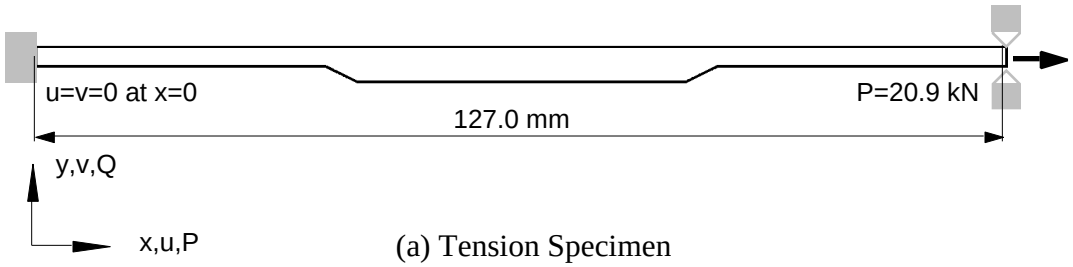

(a) Tension Specimen

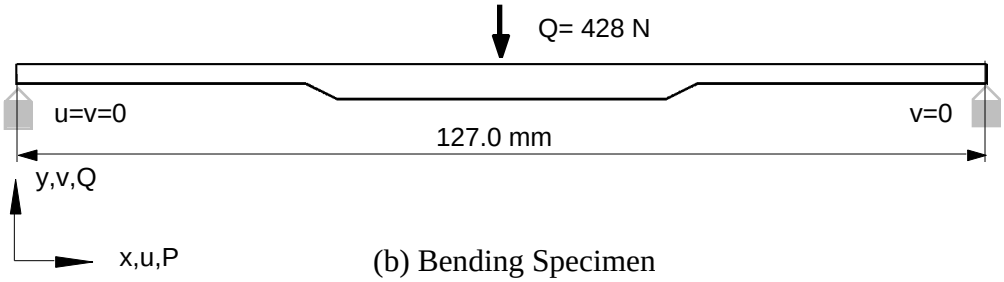

(b) Bending Specimen

Figure 17. Loads and Boundary Conditions For Tension and Three-Point Bending Case.

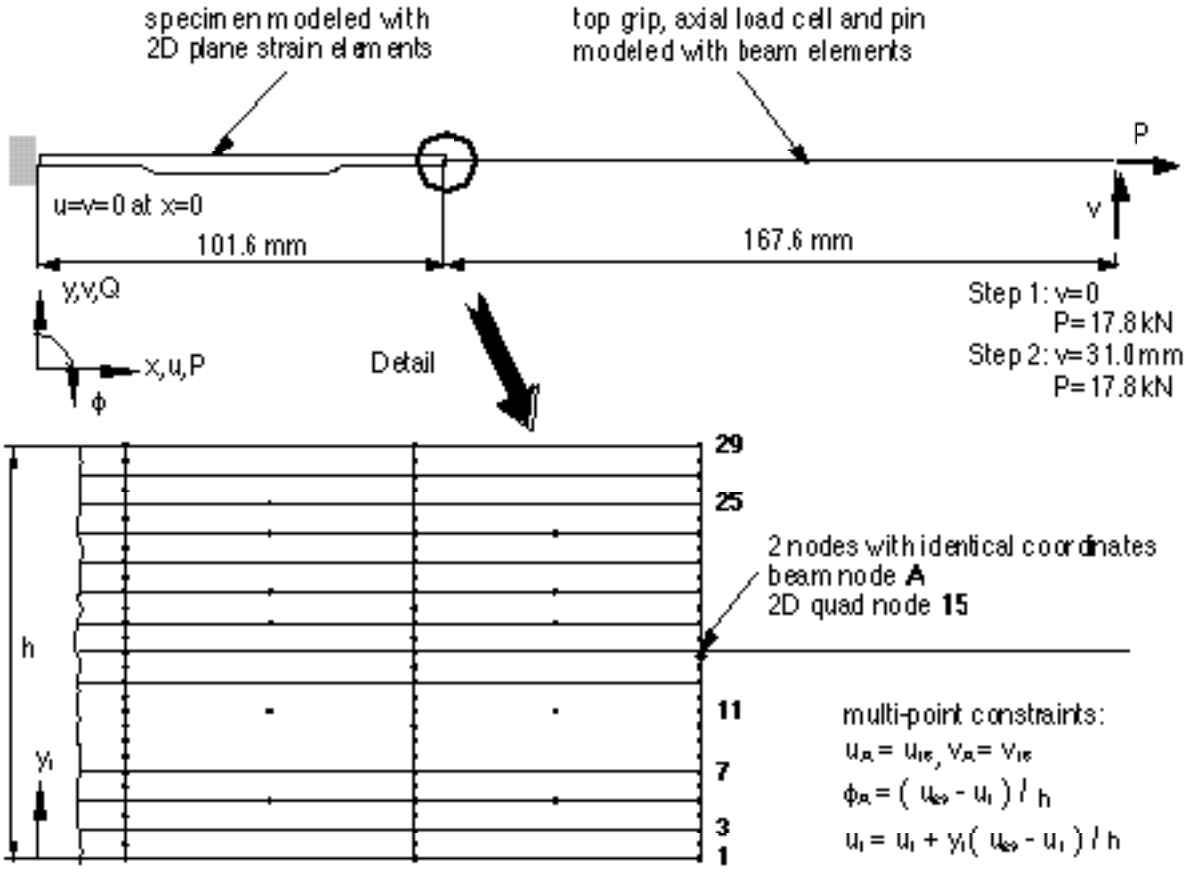

Figure 18. Loads and Boundary Conditions for ATB Test.

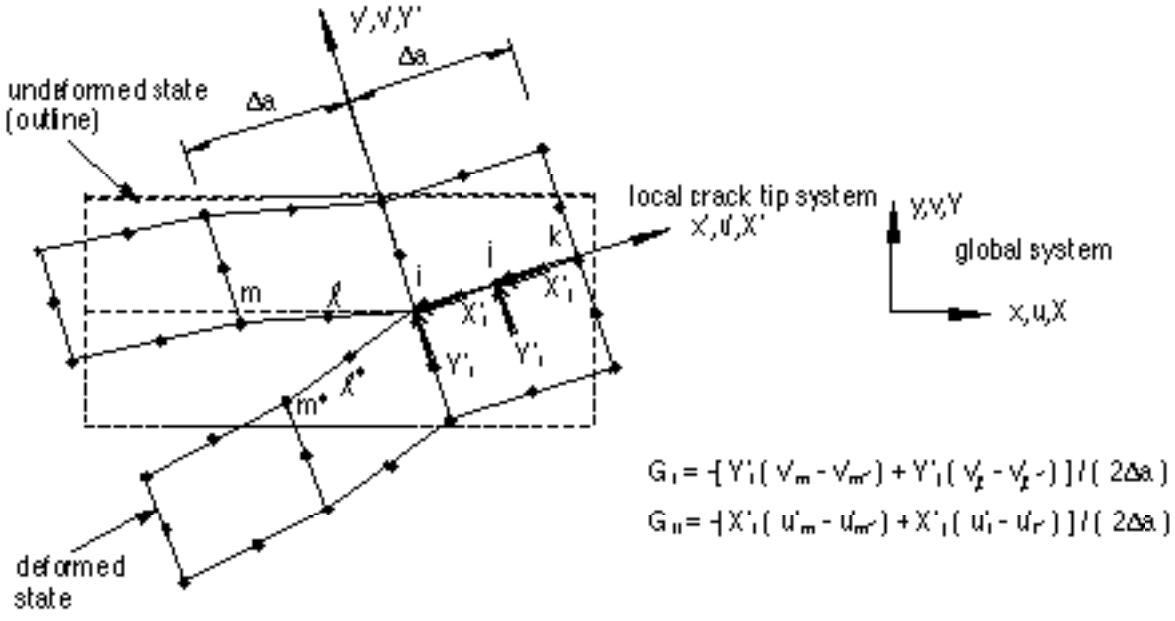

Figure 19. Virtual Crack Closure Technique (VCCT).

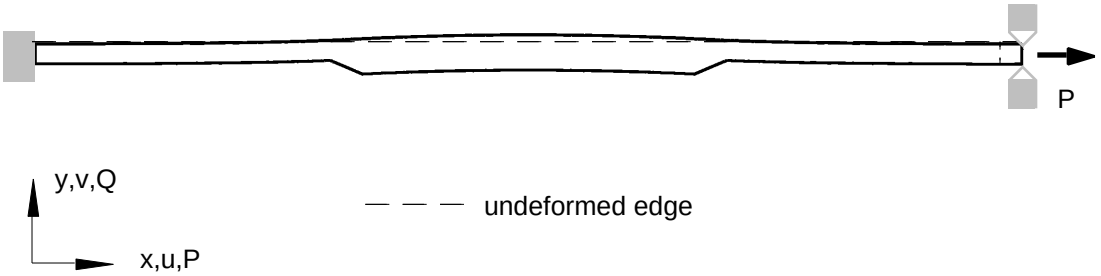

(a) Tension Specimen

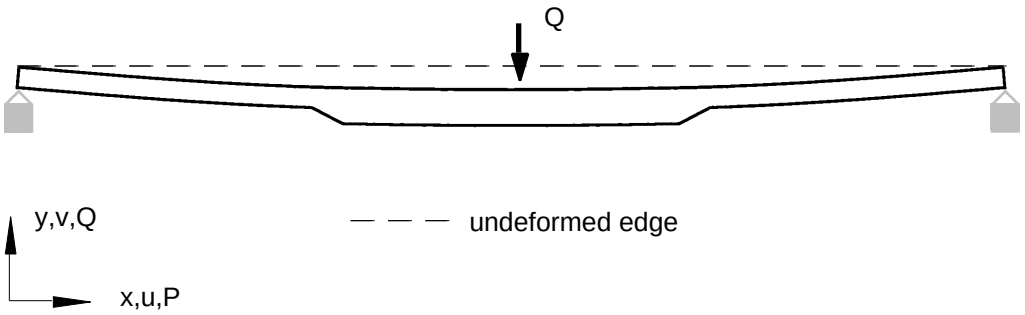

(b) Bending Specimen

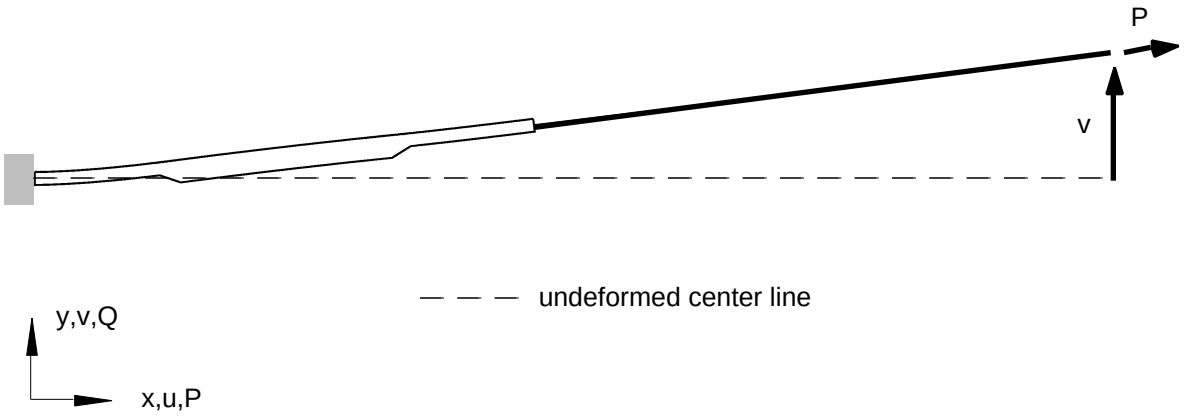

(c) ATB Specimen, Scale Different from (a) and (b)

Figure 20. Deformed Test Specimen Geometries

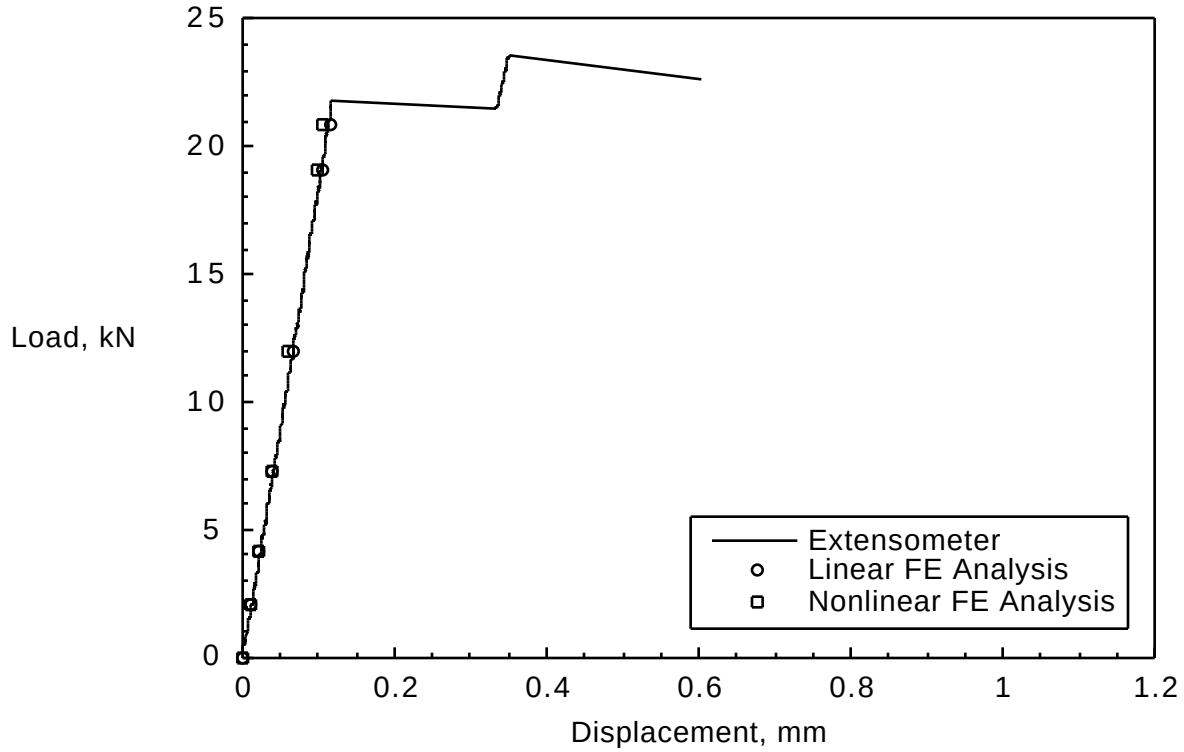

Figure 21. Comparison of Experimentally Measured Displacements with Computed Results for Tension Load Case.

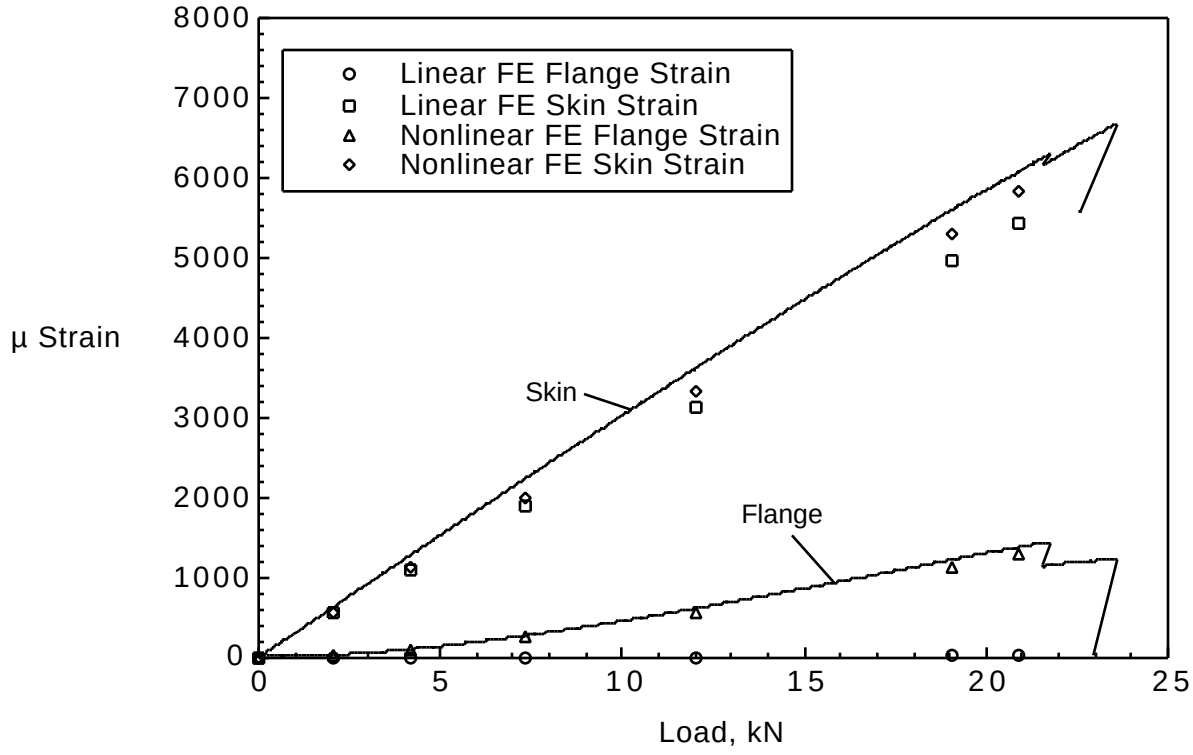

Figure 22. Comparison of Experimentally Measured Strains with Computed Results for Tension Load Case.

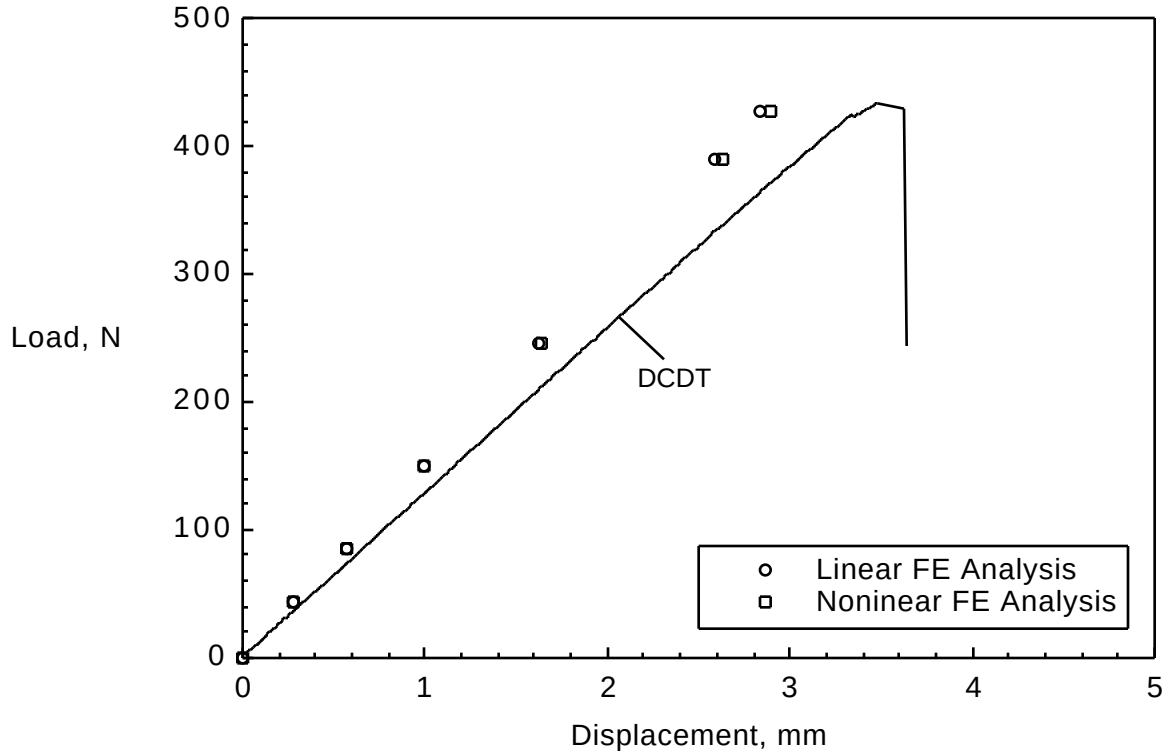

Figure 23. Comparison of Experimentally Measured Displacements with Computed Results for Three-Point Bending Load Case.

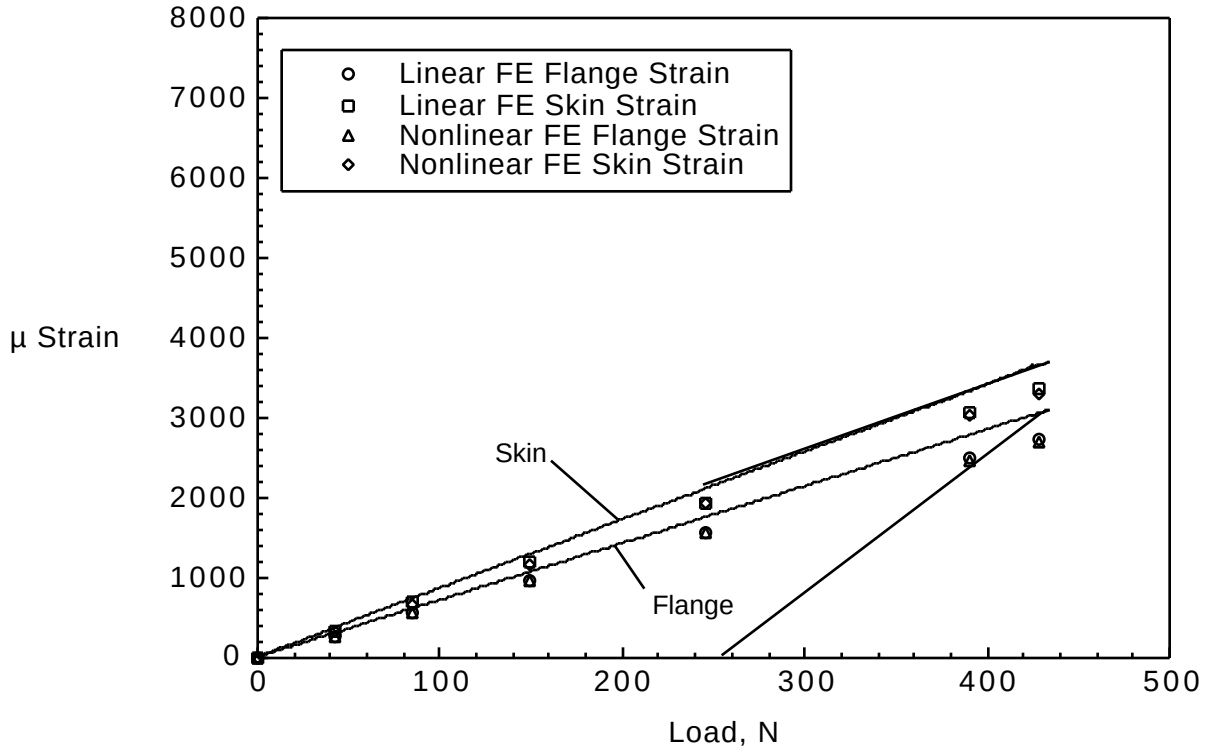

Figure 24. Comparison of Experimentally Measured Strains with Computed Results for Three-Point Bending Load Case.

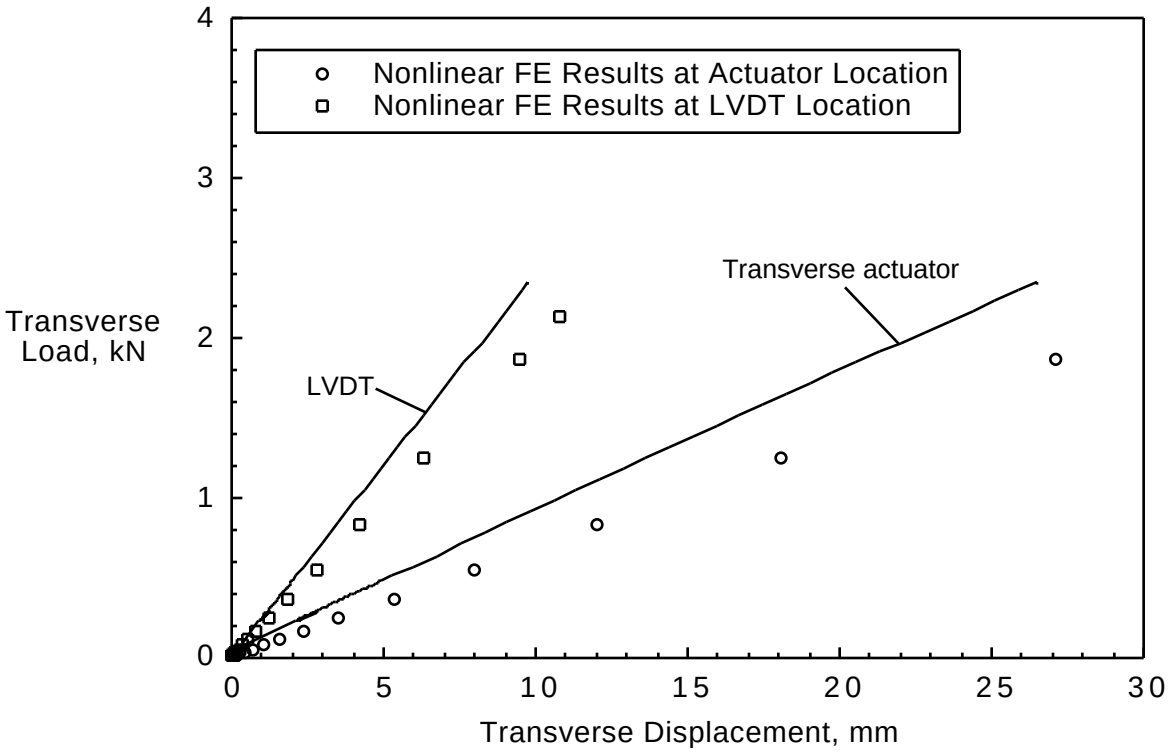

Figure 25. Comparison of Experimentally Measured Displacements with Computed Results for ATB Load Case.

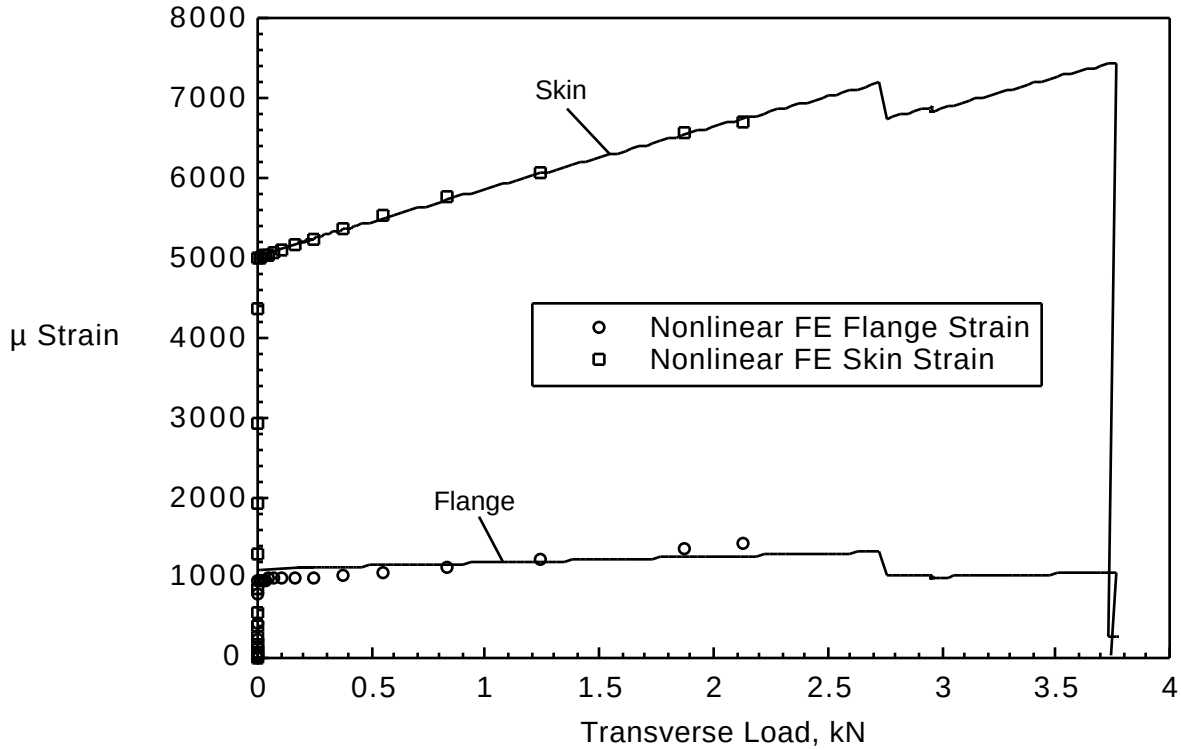

Figure 26. Comparison of Experimentally Measured Strains with Computed Results for ATB Load Case.

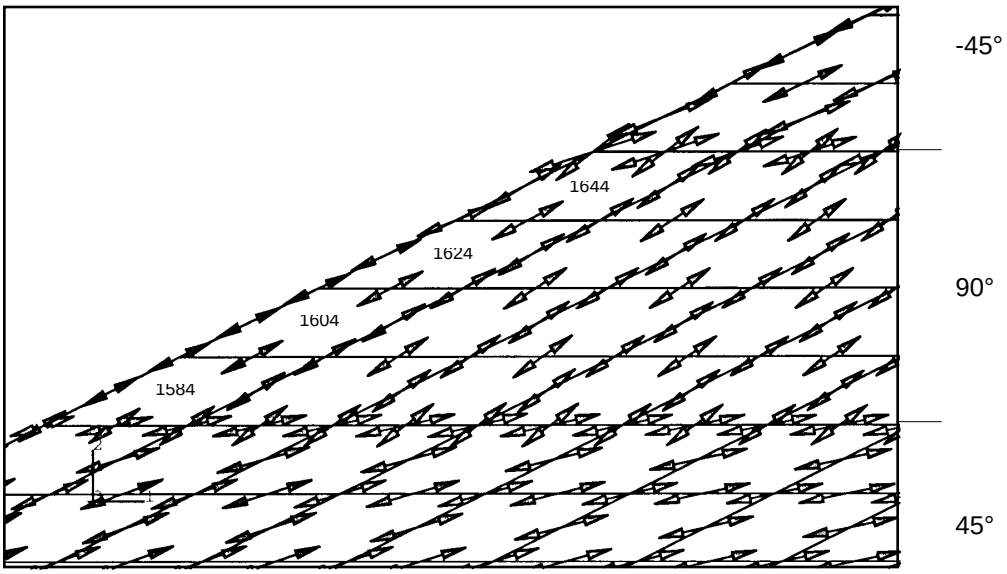

Figure 27. Trajectories of Maximum Principal Stresses.

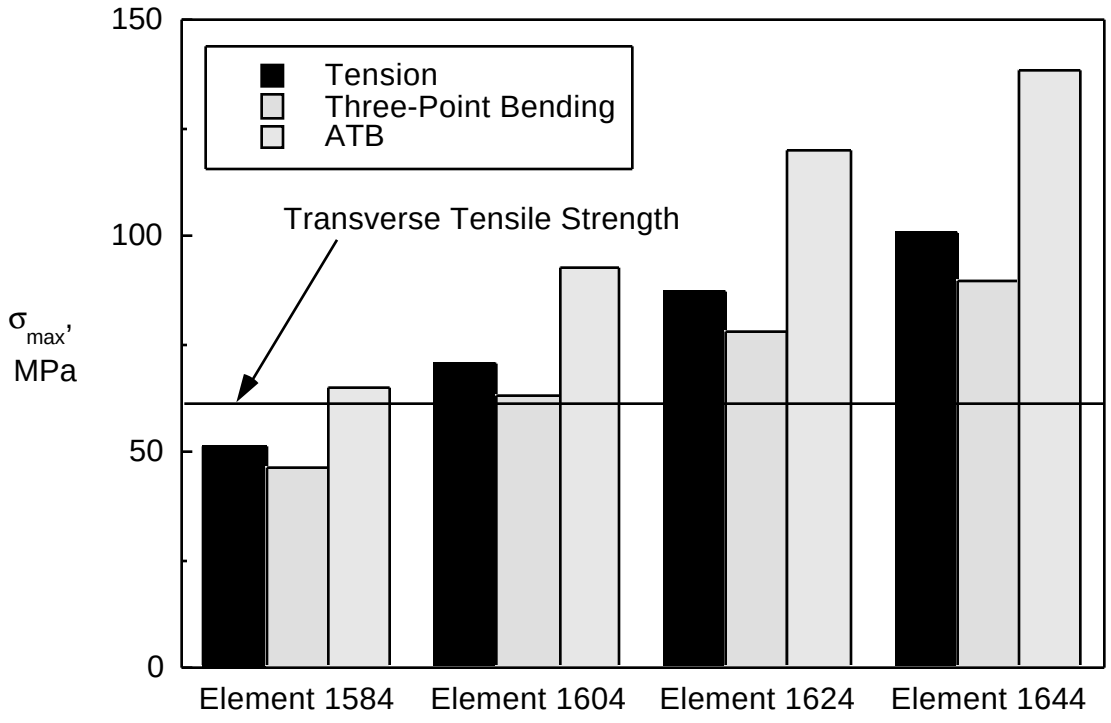

Figure 28. Comparison of Computed Principal Stresses.

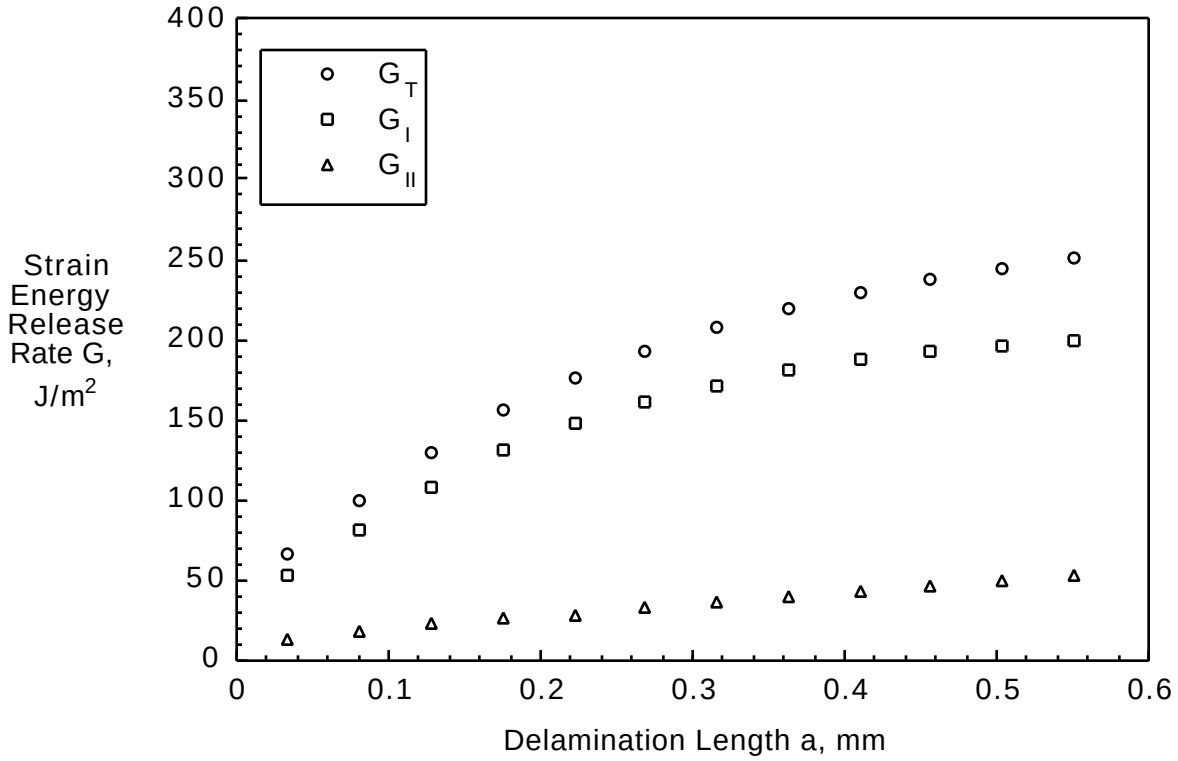

Figure 29. Computed Strain Energy Release Rates for Delamination Growth in a 90°/45° Flange Ply Interface for Tension Tests.

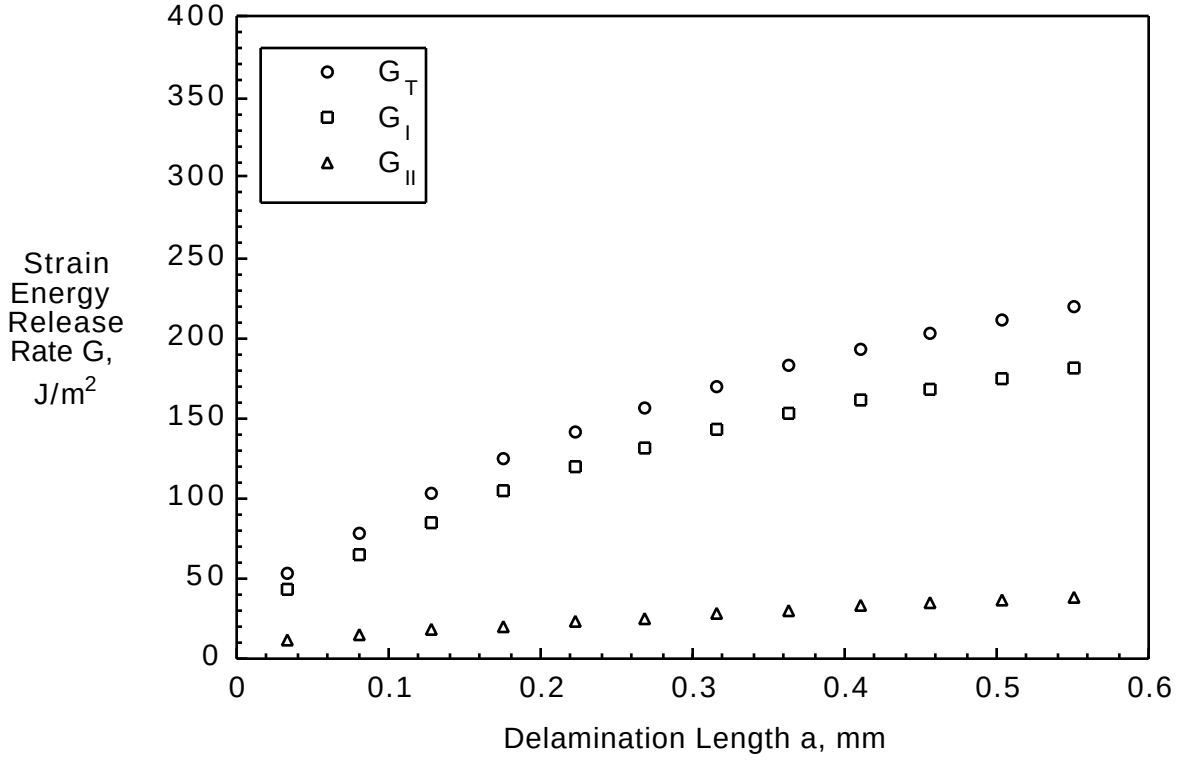

Figure 30. Computed Strain Energy Release Rates for Delamination Growth in a 90°/45° Flange Ply Interface for Three-Point Bending Tests.

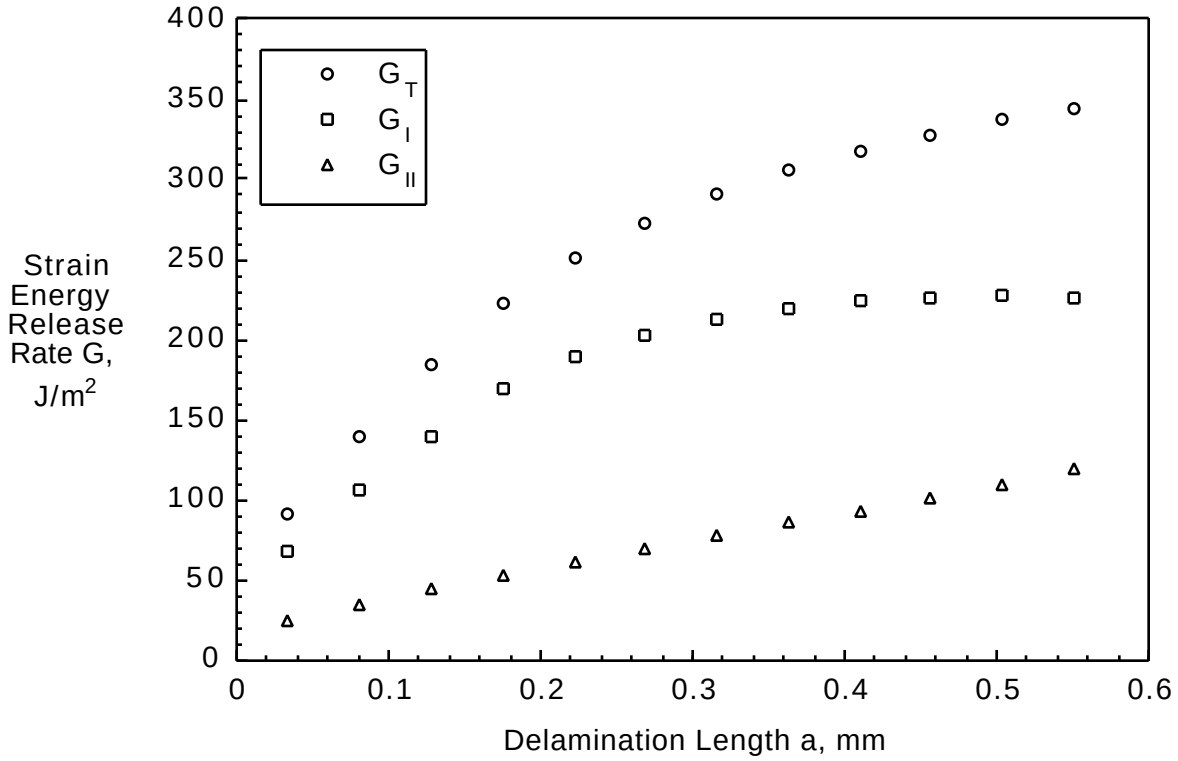

Figure 31. Computed Strain Energy Release Rates for Delamination Growth in a 90°/45° Flange Ply Interface for ATB Tests.

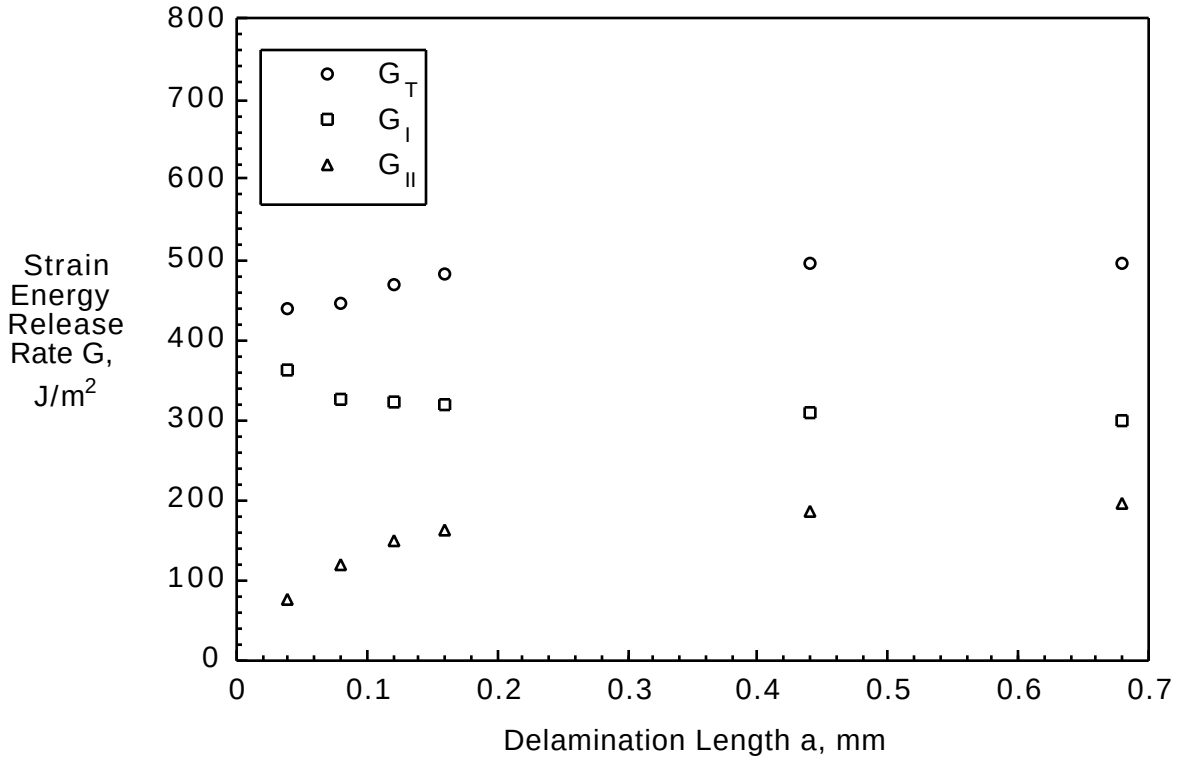

Figure 32. Computed Strain Energy Release Rates for Delamination Growth Between Adhesive and 0° Skin Ply for Tension Tests.

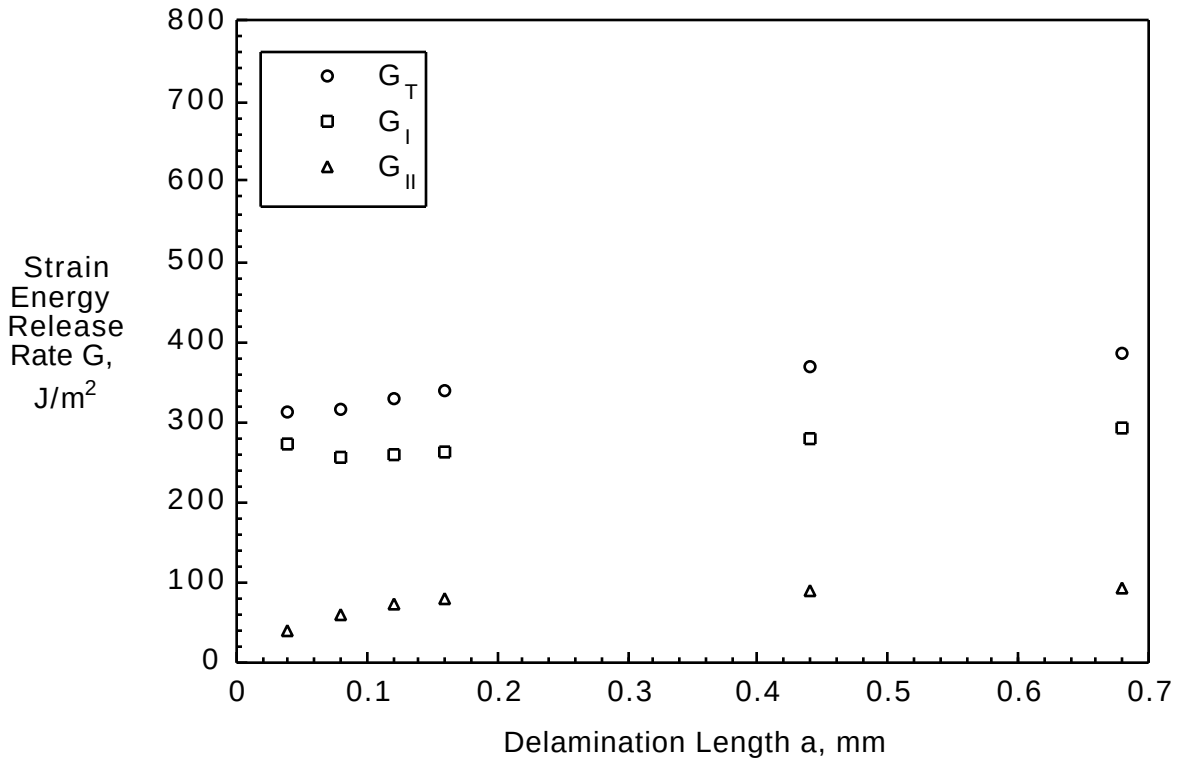

Figure 33. Computed Strain Energy Release Rates for Delamination Growth Between Adhesive and 0° Skin Ply for Three-Point Bending Tests.

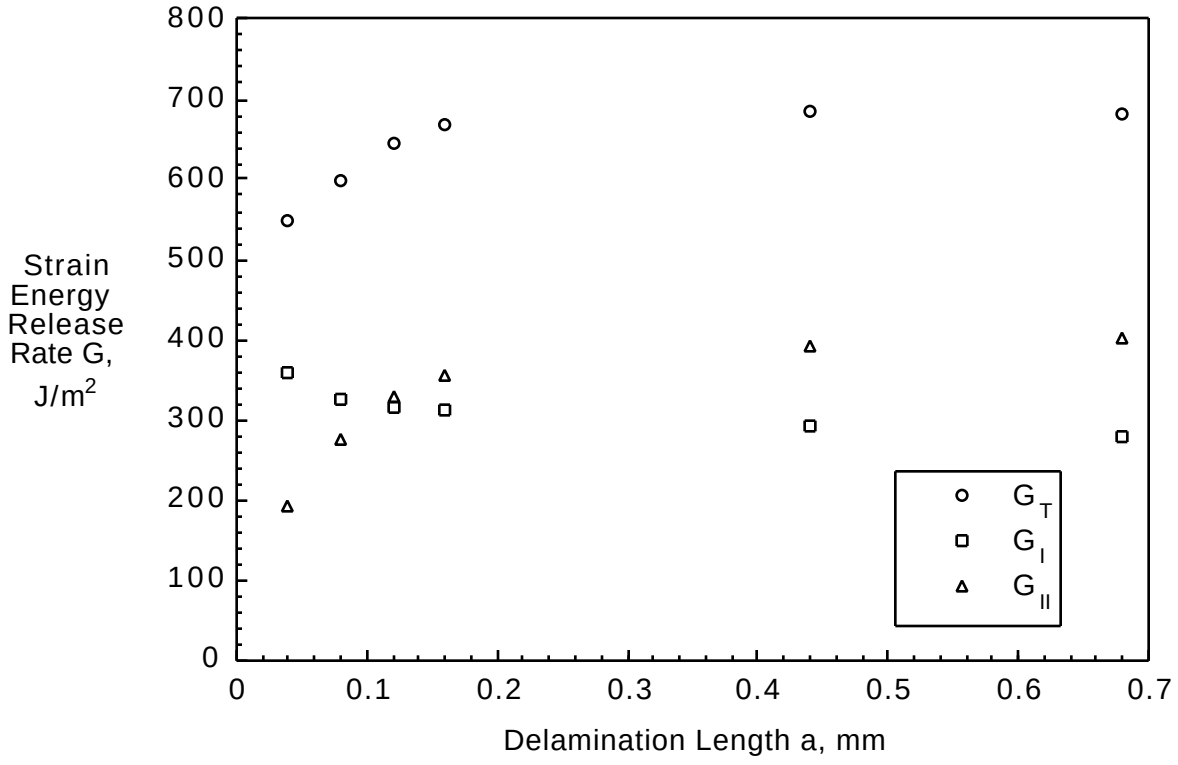

Figure 34. Computed Strain Energy Release Rates for Delamination Growth Between Adhesive and 0° Skin Ply for ATB Tests.

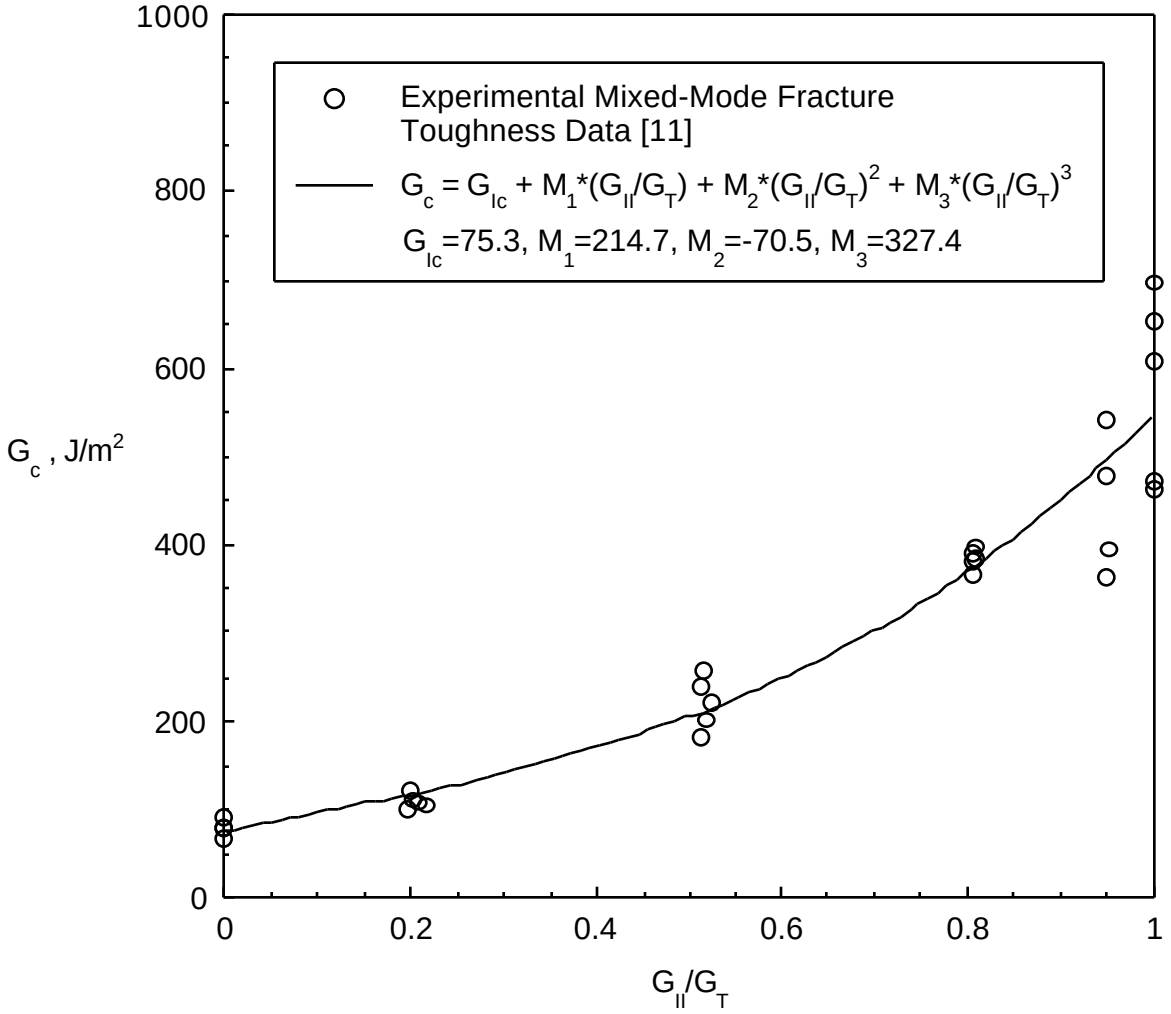

Figure 35. Mixed-Mode Delamination Criterion for AS4/3501-6 [11].

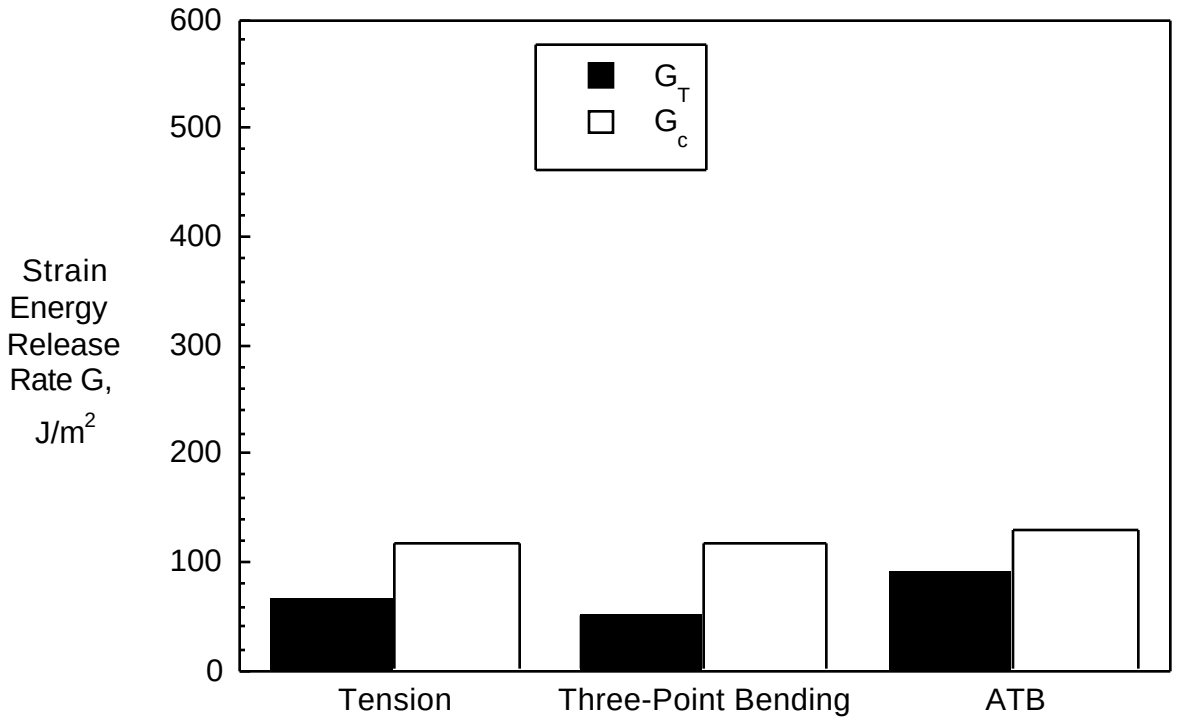

Figure 36. Comparison of Computed Total Strain Energy Release Rates with Mixed-Mode Fracture Toughnesses in a 90°/45° Flange Ply Interface.

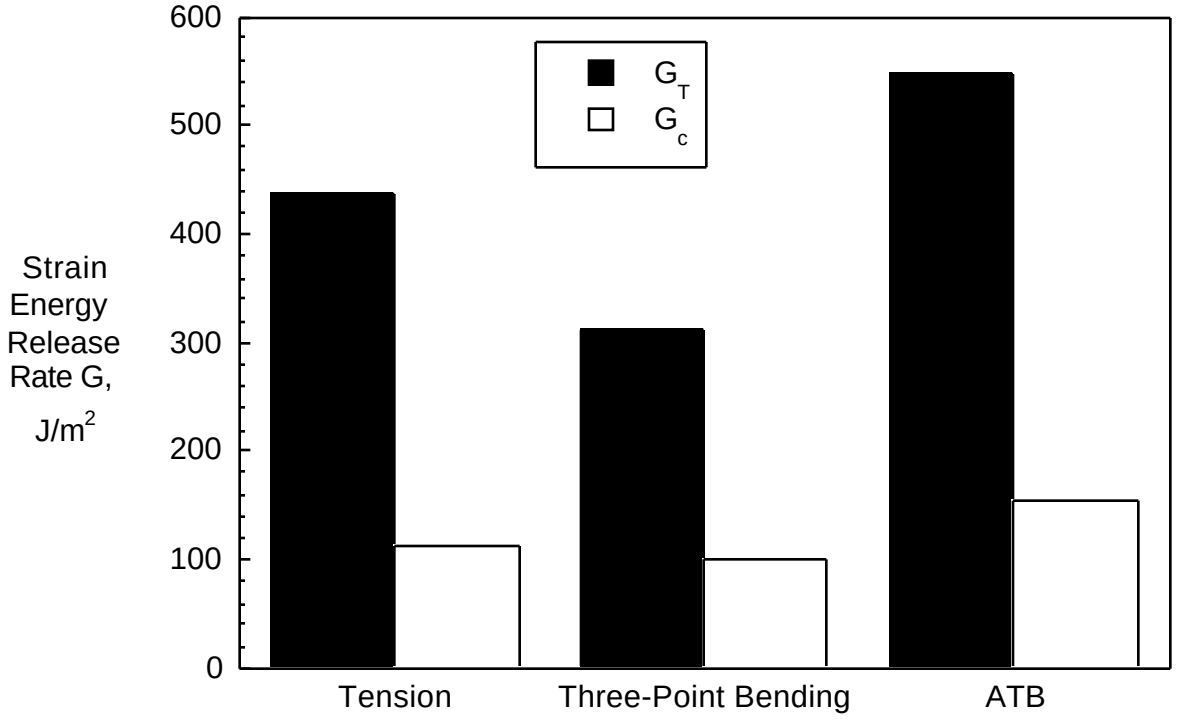

Figure 37. Comparison of Computed Total Strain Energy Release Rates with Mixed-Mode Fracture Toughnesses in a 0° Skin Ply/Adhesive Film Interface.